The Astrophysical Journal, 696:636–652, 2009 May 1 doi:10.1088/0004-637X/696/1/636

COLLAPSE BARRIERS AND HALO ABUNDANCE: TESTING THE EXCURSION SET ANSATZ

Brant E. Robertson[1,2,4], Andrey V. Kravtsov[1,2], Jeremy Tinker[1,5], and Andrew R. Zentner[3]
[1] Kavli Institute for Cosmological Physics, and Department of Astronomy and Astrophysics, University of Chicago, 933 East 56th Street, Chicago, IL 60637, USA
[2] Enrico Fermi Institute, 5640 South Ellis Avenue, Chicago, IL 60637, USA
[3] Department of Physics and Astronomy, University of Pittsburgh, Pittsburgh, PA 15260, USA
Received 2008 December 8; accepted 2009 February 2; published 2009 April 17

ABSTRACT

Our heuristic understanding of the abundance of dark matter halos centers around the concept of a density threshold, or "barrier," for gravitational collapse. If one adopts the ansatz that regions of the linearly evolved density field smoothed on mass scale M with an overdensity that exceeds the barrier will undergo gravitational collapse into halos of mass M, the corresponding abundance of such halos can be estimated simply as a fraction of the mass density satisfying the collapse criterion divided by the mass M. The key ingredient of this ansatz is therefore the functional form of the collapse barrier as a function of mass M or, equivalently, of the variance $\sigma^2(M)$. Several such barriers based on the spherical, Zel'dovich, and ellipsoidal collapse models have been extensively discussed. Using large-scale cosmological simulations, we show that the relation between the linear overdensity and the mass variance for regions that collapse to form halos by the present epoch resembles expectations from dynamical models of ellipsoidal collapse. However, we also show that using such a collapse barrier with the excursion set ansatz predicts a halo mass function inconsistent with that measured directly in cosmological simulations. This inconsistency demonstrates a failure of the excursion set ansatz as a physical model for halo collapse. We discuss implications of our results for understanding the collapse epoch for halos as a function of mass, and avenues for improving consistency between analytical models for the collapse epoch and the results of cosmological simulations.

Key words: dark matter – galaxies: formation – galaxies: halos – methods: *N*-body simulations

Online-only material: color figures

1. INTRODUCTION

A central concept in the modern theory of galaxy formation is the connection between characteristics of the linear density field and the abundance and properties of virialized dark matter halos in the contemporary universe. The power spectrum of density perturbations seeded by inflation (e.g., Guth & Pi 1982; Bardeen et al. 1983; Starobinsky 1983) and the cosmological transfer function (e.g., Peebles 1982; Bardeen et al. 1986; Eisenstein & Hu 1998) determine the character of the subsequent nonlinear growth of structure through gravitational clustering (White & Rees 1978). Growing perturbations in the initial density field serve as the sites of galaxy formation (e.g., Peebles 1965; Sachs & Wolfe 1967; White & Rees 1978). In the context of a cold dark matter cosmology, these processes give rise to the characteristic mass scale of observed galaxies (Rees & Ostriker 1977; Blumenthal et al. 1984). Cosmological observations have both motivated and verified this picture, most recently with measurements of galaxy clustering (e.g., Percival et al. 2007), the linear power spectrum of cosmological structures (e.g, McDonald et al. 2006), and high-precision measurements of the cosmological microwave background radiation (e.g., Dunkley et al. 2008).

Methods for calculating the abundances of nonlinear, collapsed structures have been developed to link the growth of density perturbations with the observed number densities of galaxy- and cluster-scale objects. Dynamical models for the collapse of individual dense patches into virialized structures, such as the spherical collapse (Gunn & Gott 1972; see Appendix A) and ellipsoidal collapse (Eisenstein & Loeb 1995; Bond & Myers 1996; see Appendix B) models, provide physically motivated methods for estimating the necessary, linearly extrapolated overdensity (the "collapse barrier") for a region to break from the cosmic expansion, condense, and form a high-density, virialized structure (i.e., a dark matter halo). When combined with the statistics of the initial density field, the collapse barrier can thereby be utilized to estimate the abundance of dark matter halos as a function of mass and redshift. The purpose of this paper is to re-examine the connection between the collapse barrier and halo abundance, and test the common assumptions and methodologies used to calculate the mass function of dark matter halos from a dynamical model for their collapse (e.g., the "excursion set" formalism, Bond et al. 1991).

Press & Schechter (1974) first used the spherical collapse model to calculate the abundance of galaxies. They assumed the probability distribution function $dP(\delta_{\rm R})/d\delta_{\rm R}$ (PDF) of the smoothed overdensity field $\delta_{\rm R} = (\rho_m - \bar{\rho}_m)/\bar{\rho}_m$, where the mean matter density is $\bar{\rho}_m$ and the density is averaged over a region of typical size R containing mass $M \propto \bar{\rho}_m R^3$, was a Gaussian with a scale-dependent variance $\sigma^2(M)$. They integrated this Gaussian PDF above the typical collapse overdensity δ_c (i.e., $P(\delta_{\rm M} > \delta_c) \propto {\rm erfc}[-\delta_c/\sqrt{2}\sigma(M)]$) and differentiated with respect to mass M (i.e., $dP/dM \propto \exp[-\delta_c^2/2\sigma^2(M)] \times d\sigma^{-1}/dM$) to arrive at the fraction of all mass contained in objects of mass M. The Press & Schechter (1974) calculation accounts for only half of the total universal mass density in bound objects because it does not address underdense regions contained within still larger regions for which the threshold $\delta_{\rm M} > \delta_c$ is satisfied. To remedy this shortcoming, Press & Schechter (1974) multiplied their final answer by a factor of 2 to account for all mass with little justification.

Bond et al. (1991) studied the properties of sets of regions above the threshold, the "excursion sets" of the density field.

[4] Spitzer Fellow.
[5] Current Address: Berkeley Center for Cosmological Physics, University of California, Berkeley, USA.

Using the excursion set formalism, Bond et al. (1991) demonstrated that by filtering the initial overdensity field on a variety of mass scales, the results of Press & Schechter (1974) could be derived in a manner that accounts for patches of low density embedded in large, high-density regions collapsing on larger scales (the "cloud-in-cloud" problem). Moreover, Bond et al. (1991) and Lacey & Cole (1993) showed that the excursion set formalism provided a means to compute other halo properties such as their mass acquisition histories. The excursion set theory of halo abundance was later extended by Mo & White (1996) to describe their spatial clustering through the bias parameter $b^2 \equiv \xi_{hh}/\xi_m$ relating the halo (ξ_{hh}) and mass (ξ_m) correlation functions (a computation that recovers the "peak-background split" result developed in Kaiser 1984; Efstathiou et al. 1988; Cole & Kaiser 1989). The details of the excursion set theory are collected in the recent review by Zentner (2007).

Numerical simulations of cosmological structure formation, which were developed concurrently with the analytical collapse calculations, demonstrated that nonlinear gravitational collapse produces halo mass functions that are inconsistent with the predictions of Press & Schechter (1974). Evidence for this disagreement, as well as corresponding discord in the spatial clustering of halos, developed over twenty years (e.g., Efstathiou et al. 1988; White et al. 1993; Lacey & Cole 1994; Eke et al. 1996; Gross et al. 1998; Tormen 1998; Jing 1998, 1999; Lee & Shandarin 1999; Porciani et al. 1999; Governato et al. 1999). The inability of the simple, spherical collapse model set within the excursion set formalism to describe the results of cosmological simulations and the need for robust predictions of the abundance of halos for comparisons with observations led to accurate formulae for mass functions determined by numerical fits to the results of N-body simulations (e.g., Sheth & Tormen 1999; Jenkins et al. 2001; Warren et al. 2006, for more recent results see Tinker et al. 2008). These fitting formulae were not the results of specific dynamical models for the collapse of dark matter halos. Rather, they were developed through a practical approach of trying to reproduce accurately the results of cosmological simulations.

Additional dynamical models for the growth of structure were developed in an attempt to better reproduce simulated mass functions while retaining a comparably simple, physically motivated framework. Lee & Shandarin (1998) presented results for the halo mass function motivated by the Zel'dovich (1970) pancake collapse model, which they extended to account for the collapse of halos along each of their principal axes. Sheth et al. (2001, SMT01) argued that the functional form of the Sheth & Tormen (1999, ST99) mass function can be motivated by the ellipsoidal collapse model of Bond & Myers (1996). For a given ellipticity e and prolaticity p of the shear field about an overdensity δ, the Bond & Myers (1996) model provides a method for estimating the linearly extrapolated overdensity at collapse (the "ellipsoidal collapse barrier"). SMT01 built on a calculation by Doroshkevich (1970) to determine a probability distribution of shear ellipticities and prolaticities, which was then used to find the most-probable values for e and p as a function of $\sigma(M)$. Combining these results, SMT01 found an effective ellipsoidal collapse barrier as a function of the "peak height," $\nu_c = \delta_c/\sigma(M)$, alone. With this new, mass-dependent collapse barrier SMT01 computed a halo mass function using the excursion set prescription of Bond et al. (1991) and showed that the predicted functional form was close to that measured in cosmological simulations by ST99. The ST99 mass function has therefore become associated with the ellipsoidal collapse model.

Note, however, that the ellipsoidal collapse model predicts that the collapse barrier converges to the spherical collapse barrier $\delta_c = 1.69$ (for $\Omega_m = 1$), in the high-mass limit, because the rarest peaks have a preferentially spherical shape. SMT01, on the other hand, found that the collapse barrier had to be lowered in the high-mass limit to $\sqrt{a_{\rm ST}}\delta_c \sim 0.84\delta_c$, in order to reproduce the mass function measured in cosmological simulations (see also Sheth & Tormen 2002). Although they argued that the lower value can be motivated by the mass definition of the friends-of-friends (FOF) algorithm which they used to identify halos in simulations, this rescaling is not well justified. Indeed, it disagrees with the fact that the collapse of the highest mass halos should be described well by the spherical collapse model. We argue below the lowering of the collapse barrier is instead required by the internal inconsistencies of the excursion set ansatz and explicitly demonstrate that such inconsistencies persist for a wide variety of halo mass definitions, including the FOF and spherical overdensity criteria (see Appendix D for a detailed discussion).

In the context of the excursion set formalism, the adoption of a shape for the collapse barrier (along with choice of prescription with which to smooth the density field) effectively determines the mass function. In this paper we test the excursion set ansatz by measuring the effective collapse barrier for halos formed in cosmological simulations and comparing excursion set predictions for the halo abundance given such a barrier to the halo mass functions measured in the simulations.

The organization of this paper is as follows. In Section 2, we review the theoretical background of the excursion set formalism, common dynamical models, and collapse barriers from the literature. In Section 3, we measure the linear overdensity of collapsed regions in cosmological simulations to study the consistency between the simulated collapse of halos and the predictions of dynamical models. We then compare the abundance of dark matter halos predicted from the excursion set formalism and dynamical models with the simulated halo mass function in Section 4. We discuss our results in Section 5 and summarize our results and conclusions in Section 6. The paper contains four appendices: a review of the spherical collapse model (Appendix A), a review of the Bond & Myers (1996) ellipsoidal collapse model (Appendix B), a summary of the Zhang & Hui (2006) analytical method for calculating the excursion set mass function (Appendix C), and a study of the connection between the excursion set ansatz and the halo mass definition (Appendix D). Unless noted otherwise, throughout the paper we assume a flat Λ-Cold Dark Matter (ΛCDM) cosmology. Cosmological parameters in our calculations and simulations are close to the values suggested by observations: $\Omega_m \approx 0.3$, $\Omega_\Lambda \approx 0.7$, and $H_0 \approx 70$ km s^{-1}Mpc^{-1}.

2. THEORETICAL BACKGROUND

Consider a Gaussian random density field $\rho(\mathbf{x})$ as a function of spatial location $\mathbf{x}$ with mean matter density $\bar{\rho}_m$. At every location $\mathbf{x}$ we can define the overdensity $\delta(\mathbf{x}) \equiv [\rho(\mathbf{x}) - \bar{\rho}_m]/\bar{\rho}_m$ of the field and the overdensity smoothed on a comoving length scale $R_{\rm W}$ as

$$\delta_{R_{\rm W}}(\mathbf{x}) = \int d^3x' \delta(\mathbf{x}') W(|\mathbf{x} - \mathbf{x}'|, R_{\rm W}) \quad (1)$$

where $W(\mathbf{x}, R_{\rm W})$ is a spherically symmetric smoothing window with a characteristic radius $R_{\rm W}$ centered about location $\mathbf{x}$. Here,

we follow the notation in the recent review by Zentner (2007) but use the symbol δ_{R_W} to represent the overdensity field smoothed on a scale R_W and reserve δ to represent the unsmoothed overdensity field. The smoothed overdensity field $\delta_{R_W}(\mathbf{x})$ is also a Gaussian random field with a variance given by

$$S(M) \equiv \sigma^2(M) \equiv \left\langle \delta^2_{R_W}(\mathbf{x}) \right\rangle = \int \Delta^2(k) |\hat{W}(k, R_W)|^2 d\ln k, \tag{2}$$

where $\Delta^2(k) = k^3 P(k)/2\pi^2$ is the dimensionless power spectrum of density fluctuations with a wavenumber k and $\hat{W}(k, R_W)$ is the Fourier transform of the real-space smoothing window $W(\mathbf{x}, R_W)$. The details of both the averaging procedure and the mass-radius relation are fixed by the choice of filtering function used to smooth the density field. In CDM models the variance monotonically decreases with increasing length or mass scale. Consequently, once the filter function is specified this variance can also be used to label the size of the smoothing region, and we can write δ_{R_W} as δ_M or δ_S where M is the mass contained within the window of length scale R_W and S is the variance $\sigma^2(M)$. In what follows, we adopt the common practice of labeling the size of the smoothing region by either the length scale R_W, the corresponding mass scale M, or the variance S, and use the labels interchangeably.

If we consider a fixed location $\mathbf{x}$ and monitor the behavior of the smoothed overdensity $\delta_S(\mathbf{x})$ as we decrease the mass smoothing scale M from some very large value (and hence increase the variance S from some value $\ll \delta_c^2$), $\delta_S(\mathbf{x})$ will execute a (not necessarily Markovian) random walk where the smoothed overdensity $\delta_S(\mathbf{x})$ will satisfy the Langevin equation (e.g., Bond et al. 1991, see also Chandrasekhar 1943)

$$\frac{\partial \delta_S(\mathbf{x})}{\partial \ln k} = Q(\ln k)\hat{W}(k, R_W), \tag{3}$$

where $Q(\ln k)$ is a Gaussian random variable with zero mean and variance

$$\left\langle Q^2(\ln k) \right\rangle = \frac{dS}{d\ln k} = \Delta^2(k). \tag{4}$$

The variation represents an ensemble of local realizations of the density field.

For a sharp k-space top-hat filter of the form

$$\hat{W}_k(k, R_W) = \Theta(1 - kR_W), \tag{5}$$

$$\Theta(x) \equiv \begin{cases} 0 & : \quad x < 0 \\ \frac{1}{2} & : \quad x = 0 \\ 1 & : \quad x > 0 \end{cases}, \tag{6}$$

the "trajectory" of overdensity as a function of variance $\delta_S(\mathbf{x})$ recovered by integrating Equation (3) will be a Markovian random walk because each Fourier coefficient of the Fourier-transformed density field is an independent random variable (e.g., Lacey & Cole 1993). More generally, the trajectory may vary more smoothly as the variance is increased if the Fourier transform of the real-space window function has broad side lobes in k-space (e.g., Zentner 2007). For instance, the real-space top-hat filter, given by

$$W_r(R, R_W) = \left(\frac{4\pi}{3} R^3\right)^{-1} \Theta(1 - R/R_W), \tag{7}$$

with Fourier transform

$$\hat{W}_r(k, R_W) = \frac{3\,(\sin kR_W - kR_W \cos kR_W)}{(kR_W)^3}, \tag{8}$$

has extended side lobes in k-space that correlate the smoothed overdensities over a considerable range of smoothing scales. Hence, the integral of Equation (3) will vary more smoothly with the variance S if a real-space top hat is used rather than a k-space top hat.

2.1. Collapse Barriers and Halo Formation

The excursion set theory of halo abundance, clustering, and formation is based on an ansatz that the locations and sizes of virialized dark matter halos can be related to the properties of peaks in the initial density field at some very high initial redshift $z_{\rm init} \gg 1$, when the density field is in the linear regime ($\delta_M \ll 1$). Almost universally, the specific form of this ansatz is that a region will collapse and form a dark matter halo if its smoothed overdensity, evolved forward in time from $z_{\rm init}$ according to linear perturbation theory, exceeds some threshold value. Consider an object that collapses at some redshift $z_c < z_{\rm init}$. The linearly extrapolated overdensity is

$$\delta_{R_W}(\mathbf{x}, z_c) = \delta_{R_W}(\mathbf{x}, z_{\rm init}) D(z_c)/D(z_{\rm init}), \tag{9}$$

where $D(z)$ is the linear growth function, given by

$$D(z) = D_0 H(z) \int_z^\infty \frac{(1+z')\,dz'}{H^3(z')}. \tag{10}$$

The Hubble parameter

$$H(z) = H_0 \left[\Omega_m (1+z)^3 + (1 - \Omega_m - \Omega_\Lambda)(1+z)^2 + \Omega_\Lambda\right]^{1/2} \tag{11}$$

describes the rate of change of the universal scale factor as $H \equiv \dot{a}/a$. The collapse condition is then simply

$$\delta_{R_W}(\mathbf{x}, z_{\rm init}) D(z_c)/D(z_{\rm init}) \geqslant B, \tag{12}$$

where B is referred to as the "collapse barrier." The excursion set ansatz is specifically that the largest smoothing scale $R_W \propto (M/\bar{\rho}_m)^{1/3}$ at any point $\mathbf{x}$ for which Equation (12) is satisfied will collapse and form a halo of mass M at redshift z_c.

The value of the collapse barrier B is usually determined by a dynamical model for the collapse of overdense patches in a background cosmological environment. In general, the collapse barrier need not be a single number and B can be a complicated function of the properties of the local linear density field (including its spatial derivatives), the smoothing window, and the smoothing scale. In the following sections, we study the spherical collapse and ellipsoidal collapse models for B.

Having specified the collapse condition and the form of the collapse barrier, the number of collapsed objects at a given mass M or variance S will be determined by the probability distribution $f(S)dS$ of variances where random realizations of trajectories $\delta_S(\mathbf{x})$, computed according to Equation (3), first cross the barrier B. This first-crossing distribution can be determined using a Monte Carlo procedure. By integrating Equation (3) for many locations in the density field (corresponding to many realizations of $Q(\ln k)$), the first-crossing distribution may be approximated by a histogram of the barrier crossings as a function of S for the ensemble of trajectories. The first-crossing distribution is often written as a function of the peak height

$$\nu_c = \delta_c/\sigma(M), \tag{13}$$

where $\delta_c = 1.686$ is the linear overdensity for spherical collapse in an $\Omega_m = 1$ cosmology (see Appendix A below for details). We will frequently change variables from S to ν_c so that we can discuss and plot the first-crossing distribution in terms of $f(\nu_c)$.

The comoving abundance of halos $(dn/dM) \times \Delta M$ in the mass range ΔM about mass M (the "mass function") is related to the first-crossing distribution $f(\nu_c)$ by

$$\frac{dn}{dM}\Delta M = \frac{\bar{\rho}_m}{M} f(\nu_c) \left|\frac{d\nu_c}{dM}\right| \Delta M. \quad (14)$$

This correspondence between the mass function and first-crossing distribution can be understood as a variable change from a distribution in peak height ν_c to a distribution in mass M, with a normalization that accounts for the partitioning of mass elements into halos of mass M (i.e., $\bar{\rho}_m/M$). The shape of the first-crossing distribution $f(\nu_c)$ is expected to be relatively independent of the cosmological model at low redshift because it depends primarily on the primordial power spectrum, the collapse barrier B, and the smoothing window (e.g., ST99). The halo abundance dn/dM additionally depends on how the relation between the trajectory mass smoothing scale M and the actual halo mass is defined and the shape of the power spectrum $P(k)$ (through $d\sigma^2/dM$). When necessary, we will associate halos with roughly virialized regions of size R_{200} with a mean physical overdensity $\Delta = 200$ (to ease comparison with the mass definition used by Tinker et al. 2008, which is defined relative to the background density, and not the critical density) and virial mass $M_{200} = 4\pi\Delta\bar{\rho}_m R_{200}^3/3$. However, we explore variations on this definition for completeness (see Appendix D).

2.2. Spherical Collapse Barrier

Gunn & Gott (1972) modeled the dynamical evolution of an overdense spherical region in a background cosmology (their calculation is detailed in Appendix A). The collapse barrier is computed by evolving the density in the spherical region according to the linear theory until the time of collapse. The final step in calculating the excursion set halo abundance from the collapse model is to assume that this equivalent linear overdensity can be used to identify collapsed regions in the initial density field without needing to consider the field's nonlinear evolution. The model predicts that a region with initial physical overdensity $\delta_S(z_{\rm init})$ will collapse when the linearly extrapolated overdensity exceeds

$$\delta_S(z) = \delta_S(z_{\rm init})D(z)/D(z_{\rm init}) > B_{\rm sc} \equiv \delta_c \approx 1.686. \quad (15)$$

We refer to the barrier δ_c as the "spherical collapse barrier." Eke et al. (1996) provide analytical solutions for the value of δ_c in cosmologies with $\Omega_m + \Omega_\Lambda = 1$. The spherical collapse barrier is independent of mass scale and initial overdensity.

Bond et al. (1991) used the excursion set formalism to calculate the first-crossing distribution associated with a barrier that is constant as a function of mass scale, such as the spherical collapse barrier. For a sharp-k window function (Equation (5)), the spherical collapse barrier first-crossing distribution is

$$\nu_c f_{\rm sc}(\nu_c) = 2\left(\frac{\nu_c^2}{2\pi}\right)^{1/2} \exp\left(-\frac{\nu_c^2}{2}\right). \quad (16)$$

The function $f_{\rm sc}$ is normalized such that $\int f_{\rm sc}(\nu_c)d\nu_c = 1$, implying that all mass in the universe is incorporated into collapsed objects. In this context, the normalization arises because the variance $S = \sigma^2(M)$ increases monotonically toward infinity as M tends toward zero, while the barrier height δ_c, remains fixed. As a result, any random walk will cross the barrier δ_c at some scale.

2.3. Ellipsoidal Collapse Barrier

The spherical collapse model is likely too simplistic because peaks in the linear density field are, in general, locally triaxial (see, e.g., Doroshkevich 1970; Bardeen et al. 1986). A number of dynamical collapse models designed to account for deviations from spherical symmetry have been explored (e.g., Zel'dovich 1970; Nariai & Fujimoto 1972; Hoffman 1986; Bertschinger & Jain 1994; Eisenstein & Loeb 1995; Bond & Myers 1996; Audit et al. 1997; Del Popolo et al. 2001; Shen et al. 2006). Bond & Myers (1996) studied an ellipsoidal collapse model that approximates peaks in the linear density field as ellipsoids and accounts for the effects of tides on the evolution of overdense patches (see Appendix B for a more detailed review of the model). Compared with the spherical case, the key feature of the ellipsoidal collapse models is that for a fixed overdensity the collapse epoch will depend on the local ellipticity and prolaticity of the shear (or possibly density) field. The net effect is that less spherical peaks have to overcome additional tidal stretching and require a higher overdensity to collapse.

SMT01 used the Bond & Myers (1996) ellipsoidal collapse model to derive the dependence of collapse overdensity on the ellipticity and prolaticity of the shear field. They found that the barrier shape could be approximated by the solution of the implicit equation

$$\frac{\delta_{\rm ec}}{\delta_c} = 1 + \beta\left[5(e^2 \pm p^2)\left(\frac{\delta_{\rm ec}^2}{\delta_c^2}\right)\right]^\gamma, \quad (17)$$

where β and γ are numerical parameters that must be fit to the results of the dynamical model and the squares of the ellipticity, e, and prolaticity, p, are summed (differenced) if $p < 0$ ($p > 0$).

Determining the shape of the ellipsoidal collapse barrier requires a further model for how the typical ellipticity or prolaticity scales with galaxy mass because the barrier shape depends explicitly on both e and p. SMT01 used the results of Doroshkevich (1970) to arrive at a PDF for e and p, from which they find the most probable prolaticity and ellipticity are $p_{\rm mp} = 0$ and $e_{\rm mp} = \sigma/\delta\sqrt{5}$, respectively. They then set $\delta = \delta_{\rm ec}$ and substituted $e_{\rm mp}$ and $p_{\rm mp}$ into Equation (17) to find

$$B_{\rm ec} \equiv \delta_{\rm ec} = \delta_c\left[1 + \beta\left(\frac{\sigma^2(M)}{\delta_c^2}\right)^\gamma\right]. \quad (18)$$

SMT01 found the parameter values $\beta \approx 0.47$ and $\gamma \approx 0.615$ (more recently, values of $\beta \approx 0.412$ and $\gamma \approx 0.618$ were found by Desjacques 2008). We refer to the threshold in Equation (18) as the "ellipsoidal collapse barrier." For reference, Figure 1 compares the ellipsoidal collapse barrier with the constant spherical collapse barrier.

SMT01 also suggested an analytical form to approximate the first-crossing distribution resulting from the barrier $\delta_{\rm ec}$, which they calculated numerically using Monte Carlo realizations of the Langevin equation (Equation (3)). They prescribed the formula

$$\nu_c f_{\rm ec}(\nu_c) = 2A\left(1 + \nu_c^{-2q}\right)\left(\frac{\nu_c^2}{2\pi}\right)^{1/2} \exp\left(-\frac{\nu_c^2}{2}\right), \quad (19)$$

where $q = 0.3$, and the constant $A = 0.3222$ is determined by requiring $\int f_{\rm ec}(\nu_c)d\nu_c = 1$.

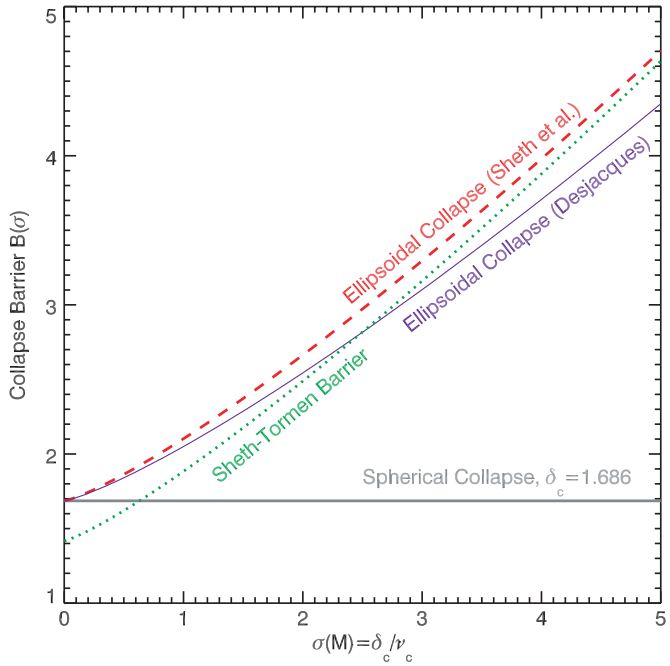

Figure 1. Some common collapse barriers discussed in the text: the spherical collapse barrier (Gunn & Gott 1972, $\delta_c \approx 1.686$ for $\Omega_m = 1$, solid gray line), the ellipsoidal collapse barrier (Sheth et al. 2001, dashed red line), an alternative fit to the ellipsoidal collapse barrier (Desjacques 2008, solid purple line), and the modified ellipsoidal collapse barrier associated with the Sheth & Tormen (1999) mass function (Sheth et al. 2001, dotted green line). Note that while the ellipsoidal collapse barriers, as formulated, converge to spherical collapse barrier at large masses (small $\sigma(M)$), the modified barrier of Sheth et al. (2001) converges to a lower value of $\sqrt{a_{\rm ST}}\delta_c \approx 0.84\delta_c$.

(A color version of this figure is available in the online journal.)

2.4. The Sheth et al. Barrier and Mass Function

To improve the agreement between the excursion set mass function determined by using Equation (18) and the abundance of halos in the GIF simulations (Kauffmann et al. 1999) measured by ST99, SMT01 introduced another parameter, $a_{\rm SMT} \approx 0.707$, to modify the ellipsoidal collapse barrier as

$$B_{\rm SMT} \equiv \delta_{\rm SMT} = \sqrt{a_{\rm SMT}}\delta_c \left[1 + \beta\left(\frac{\sigma^2(M)}{a_{\rm SMT}\delta_c^2}\right)^{\gamma}\right], \qquad (20)$$

and changed the values of the other parameters to $\beta = 0.5$ and $\gamma = 0.6$. We refer to Equation (20) as the "Sheth et al. barrier," to contrast it with the ellipsoidal collapse barrier because the changes are not based on the dynamical collapse model.

The modified barrier is lower than the $B_{\rm ec}$, with the difference increasing with increasing mass. In particular, instead of converging to the spherical collapse barrier of $\delta_{\rm ec} \to \delta_c$ at the largest masses, as expected from the trend toward sphericity for the rarest peaks, the modified barrier converges to $\delta_{\rm SMT} \approx \sqrt{a_{\rm SMT}}\delta_c \approx 0.84\delta_c$. The value $a_{\rm SMT} = 0.707$ was justified by SMT01 as accounting for the particular choice of the halo mass definition in the GIF simulations (identified by the FOF algorithm with a linking length $b = 0.2$; see the discussion in Section 4.1 of SMT01 and Appendix D). For reference, the Sheth et al. barrier is plotted in Figure 1 alongside the spherical collapse and ellipsoidal collapse barriers.

SMT01 utilized Equation (20) as the collapse barrier to calculate an excursion set mass function using Monte Carlo methods (see also Sheth & Tormen 2002), and found the resulting first-crossing distribution to be well approximated by the analytical formula

$$\nu_c f_{\rm SMT}(\nu_c) = 2A\left[1 + \left(\sqrt{a_{\rm SMT}}\nu_c\right)^{-2q}\right]\left(\frac{a_{\rm SMT}\nu_c^2}{2\pi}\right)^{1/2} \times \exp\left(-\frac{a_{\rm SMT}\nu_c^2}{2}\right), \qquad (21)$$

with $a_{\rm SMT} = 0.707$, $q = 0.3$, $A = 0.3222$. This formula was introduced by ST99 as a fit to the GIF simulations, and the corresponding halo mass function (calculated from Equation (14)) is often referred to as the "Sheth–Tormen" mass function. The normalization of the first-crossing distribution for the Sheth–Tormen mass function is the same as the spherical and ellipsoidal collapse first-crossing distributions, with $\int f_{\rm SMT}(\nu_c)d\nu_c = 1$.

3. TESTING THE COLLAPSE BARRIER WITH COSMOLOGICAL SIMULATIONS

As we have noted above, the two main ingredients of the excursion set formalism are the collapse barrier used to decide which mass elements form halos and the sampling of the possible collapse histories via the random walks of the smoothed overdensity field. Each of the elements of the excursion set approach can be tested against cosmological numerical simulations of structure formation. In particular, the correct collapse barrier, if indeed one can be defined, may be verified or falsified using numerical simulations that include all of the complications that the excursion set approach aims to circumvent. In the previous section, we described the collapse barriers motivated by the spherical and ellipsoidal collapse models, as well as the modified barrier of SMT01. In this section we compare these collapse barriers with the linear overdensities of regions that actually collapse to form halos in numerical simulations.

To calculate the linear overdensity of regions that later collapse to form dark matter halos, we utilize cosmological simulations performed with the Adaptive Refinement Tree code (ART; Kravtsov et al. 1997). One 512^3 particle simulation models the formation of structure in the *Wilkinson Microwave Anisotropy Probe* (WMAP) first-year cosmology (Spergel et al. 2003, $\Omega_m = 0.3$, $\Omega_\Lambda = 0.7$, $\Omega_b = 0.04$, $n = 1$, $\sigma_8 = 0.9$, $h = 0.7$) in a cubic volume $L = 250h^{-1}$Mpc on a side (hereafter, the L250 box). This simulation has a gravitational force resolution at the highest level of refinement of $\epsilon_{\rm L250} = 7.6h^{-1}$kpc, and a particle mass of $m_{p,\rm L250} = 9.69 \times 10^9 h^{-1} M_\odot$. An additional 1024^3 particle simulation of the WMAP third-year cosmology (Spergel et al. 2007, $\Omega_m = 0.27$, $\Omega_\Lambda = 0.73$, $\Omega_b = 0.047$, $n = 0.95$, $\sigma_8 = 0.79$, $h = 0.7$) with a larger volume ($L = 1000h^{-1}$Mpc; L1000W) is used to probe rare objects. This larger-volume simulation has a comparably coarser resolution ($\epsilon_{\rm 1000W} = 30h^{-1}$kpc, $m_{p,\rm L1000W} = 6.98 \times 10^{10} h^{-1} M_\odot$) than the smaller simulation.

The simulations analyzed in this work were recently used by Tinker et al. (2008) as part of their study of the universality of the halo mass function, and we use their halo catalogs when calculating the properties of the dark matter halo population. Tinker et al. (2008) identified dark matter halos using a modified spherical overdensity algorithm (e.g., Lacey & Cole 1994), as detailed in their Section 2.2. Halo membership at a given redshift was determined by identifying peaks in the density field and assigning dark matter particles to peaks until the maximum radius R_Δ of each halo contains a mean physical density of $\Delta = M/(4\pi\bar{\rho}_m(z)R_\Delta^3/3)$, where M is the sum of the particle

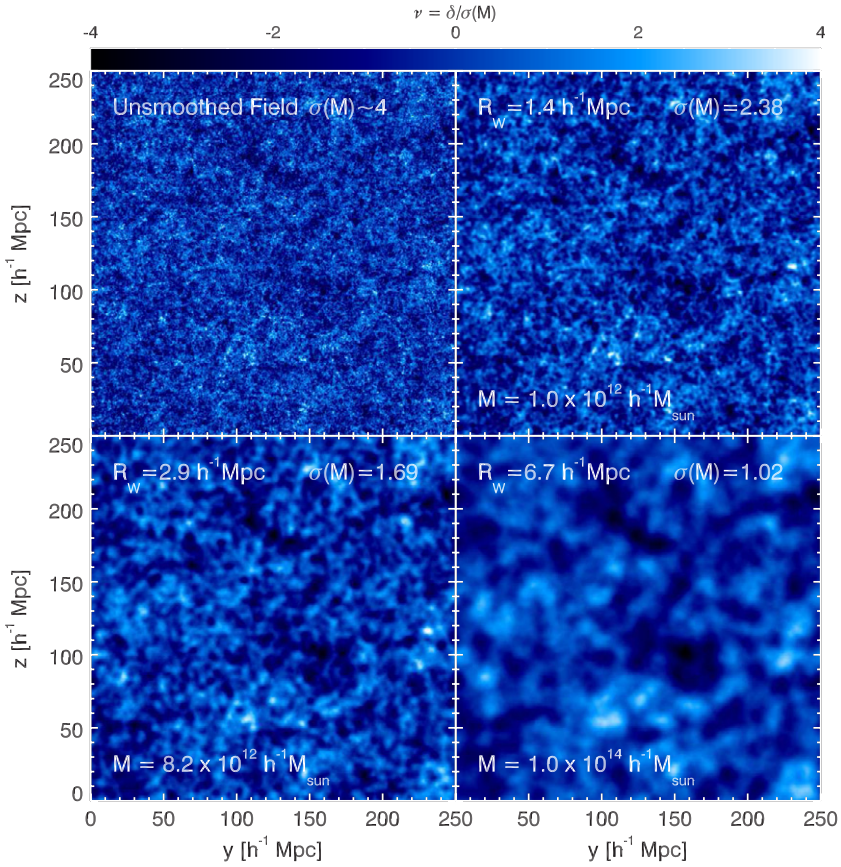

Figure 2. Linear overdensity field as a function of smoothing scale for the L250 simulation at $a = 0.01$. The upper left panel shows the linear overdensity field interpolated onto a 512^3 grid using the cloud-in-cell method (i.e., at full resolution of the simulation); the effective smoothing of this grid corresponds to $\sigma(M) \sim 4$. The other three panels show the field $\delta(\mathbf{x}, R_{\rm W})$ smoothed on larger scales $R_{\rm W}$ using a real-space top-hat window: $R_{\rm W} = 1.4h^{-1}$Mpc [$\sigma(M) = 2.38$, $M = 1.0 \times 10^{12}h^{-1}$], $R_{\rm W} = 2.9h^{-1}$Mpc [$\sigma(M) = 1.69$, $M = 8.2 \times 10^{12}h^{-1} \approx M_\star$], and $R_{\rm W} = 6.7h^{-1}$Mpc [$\sigma(M) = 1.02$, $M = 1.0 \times 10^{14}h^{-1}$].

(A color version of this figure is available in the online journal.)

masses. Results for other halo mass definitions are examined in Appendix D.

Regions in the linear density field that collapse to form halos are selected by identifying particles from the $z = 0$ halo catalog in the simulation volume at early times. For each simulation volume, we use the Zel'dovich (1970) approximation to rescale the density field at the initial epoch of the simulation ($z > 50$) to a sufficiently early epoch at which the density field can be safely considered to be linear. We choose to rescale all simulations to the scale factor $a = 0.01$. The density field for each simulation is calculated by a cloud-in-cell interpolation of the particle distribution onto a 512^3 grid. This interpolated density field has a mass resolution equal to the particle mass for the L250 box, and eight times coarser mass resolution than the L1000W box. Hence, the field is effectively smoothed on a scale of $\sigma_{\rm max}(M) \approx 4.2$ for L250 and $\sigma_{\rm max}(M) \approx 2.1$ for L1000W. We will use each box only on scales $\sigma(M) < \sigma_{\rm max}(M)$. Note that since we are interested in the regions that form collapsed halos in the Tinker et al. (2008) catalog, the largest $\sigma(M)$ of interest corresponds to the smallest halo for each simulation and all such regions are $\sigma(M) < \sigma_{\rm max}(M)$.

3.1. Smoothing the Linear Overdensity Field

The linear overdensity field smoothed on a scale $R_{\rm W}$ can be calculated directly from Equation (1) by convolving the density field with the window function $W(\mathbf{x}, R_{\rm W})$. A much more computationally efficient approach is to perform the convolution via multiplication in Fourier space to obtain the transform of the smoothed overdensity field as

$$\hat{\delta}_{R_{\rm W}}(k) = \hat{\delta}(k)\hat{W}(k, R_{\rm W}), \tag{22}$$

and then perform the inverse Fourier transform to arrive at the smoothed overdensity $\delta_{R_{\rm W}}(\mathbf{x})$. Here, $\hat{\delta}$ is the Fourier transform of the unsmoothed density field and $\hat{W}(k, R_{\rm W})$ is the transform of the window function (for instance, $\hat{W}(k, R_{\rm W}) = \hat{W}_{\rm r}$ for a real-space top hat, see Equation (8)). For each simulation volume, we compute this convolution for 150 smoothing scales from $R_{\rm W} \approx L/10$ to $R_{\rm W} \approx L/256$. This results in $512^3 \approx 134$ million overdensity trajectories with 150 steps in $\sigma(M)$, as the change of overdensity with decreasing smoothing scale at the location of each of the grid cells is equivalent to integrating Equation (3) with correlated large-scale modes. We have verified that the root-mean-squared overdensity fluctuations in each box are $\langle \delta^2_{R_{\rm W}}(\mathbf{x}) \rangle = \sigma^2(R_{\rm W})$ simply by averaging over the gridded density field, in concordance with Equation (2).

Figure 2 shows the linear overdensity field $\delta(a = 1) = \delta(a = 0.01)D(a = 1)/D(a = 0.01)$ of a thin slice through the L250 simulation volume. Shown are the unsmoothed field (upper left panel) and the field smoothed on scales of $\sigma(M) = 2.38$ ($R_{\rm W} = 1.4h^{-1}$Mpc, $M \approx 10^{12}h^{-1}M_\odot$, approximately the mass of the Milky Way halo, upper right panel), $\sigma(M) = 1.69$ ($R_{\rm W} = 2.9h^{-1}$Mpc, $M = M_\star = 8.2 \times 10^{12}h^{-1}M_\odot$, the present collapse mass scale, lower left panel), and $\sigma(M) = 1.02$

($R_W = 6.7h^{-1}$Mpc, $M \approx 10^{14}h^{-1}M_\odot$, the mass of a large group, lower right panel) using a real-space top-hat filter (Equation (7)). The figure illustrates a variety of properties of the overdensity distribution and the filter function as the smoothing scale is varied. The real-space top-hat filter is broad in Fourier space, so the variations in overdensities across many intervals in the smoothing scale are correlated. A sharp k-space filter would tend to decorrelate the overdensities on small smoothing scales from larger scales as independent frequency modes are added with increasing $\sigma(M)$. The largest fluctuations in the unsmoothed overdensity field are identifiable across the smoothed fields, reflecting the relation between the initial density fluctuations and the eventual formation of massive structures.

3.2. Smoothed Overdensities of Collapsed Regions at $z = 0$

We can use the smoothed density fields to connect the final mass of a collapsed region (and its associated fluctuation scale $\sigma(M)$) with its initial smoothed overdensity linearly extrapolated to the epoch of observation. For each halo identified in our catalogs at $z = 0$, we calculate the center-of-mass of the halo particles from their positions in the linear density field at $a = 0.01$ and use the window-smoothed field to compute the overdensity within the Lagrangian radius[6] $R = (3M/4\pi\bar{\rho}_m)^{1/3}$ about this location. This overdensity is then linearly extrapolated to $z = 0$ to serve as an estimate of $\delta_M(\mathbf{x})$. We have checked that all of our conclusions are robust to specific choices regarding the smoothing procedure, such as the choice of initial positions (the $\mathbf{x}$) of halos in the initial density field and the range of smoothing scales.

Figure 3 shows the distribution of such smoothed linear overdensities extrapolated to $z = 0$ as a function of $\sigma(M)$. The shaded regions represent the probability distribution $p(\delta, \sigma)$ for regions that collapse to form halos defined relative to a $\Delta = 200$ spherical overdensity identified in the L1000W (601,448 halos) and L250 (73,720 halos) boxes. The median (colored diamonds) and mean (colored circles) of $\delta(z = 0)$ in bins of width $\Delta\sigma(M) = 0.25$ are measured for the halo population and shown for comparison. The distribution at fixed $\sigma(M)$, $p(\delta|\sigma)$, is approximately log-normal in shape, with a width that scales as $\Sigma(\delta) \approx 0.3\sigma^{1.0}(M)$ (indicated by the error bars in Figure 3). The scatter in $\delta(z = 0)$ at fixed $\sigma(M)$ reflects both the intrinsic scatter in the linear overdensity of collapsed regions and the limitations of our method to measure $\delta(z = 0)$ reliably for any individual halo. The error on the mean or median in any $\sigma(M)$ bin is much smaller than $\Sigma(\delta)$.

At all measured halo masses, the mean and median linear overdensity of the halo population at $\delta(z = 0)$ exceeds the spherical collapse overdensity δ_c. The dependence of the mean and median overdensity on $\sigma(M)$ measured in simulations increases in a manner that resembles the functional form of the ellipsoidal collapse barrier δ_{ec} (Equation (18)) and modified Sheth et al. barrier δ_{SMT}, but with a different normalization. Importantly, at the lowest values of variance (largest masses) probed by the simulations ($\sigma(M) \sim 0.5$) *the measured overdensities of the collapsed objects are larger than both the modified Sheth et al. barrier δ_{SMT} and the spherical collapse barrier δ_c*. We note that while our $L = 1h^{-1}$GpcΛCDM simulations do not probe the highest masses ($M \gtrsim 5 \times 10^{15}\, M_\odot$) and the largest scales ($\sigma(M) \lesssim 0.4$) imaginable, in Appendix D we show that the conclusions developed from these results do not change even if the characteristic overdensity of regions that collapse to form halos does not asymptote exactly to δ_c for $\sigma \to 0$. In the next section of the paper, we explore the implication of these results for halo mass functions calculated using the excursion set formalism.

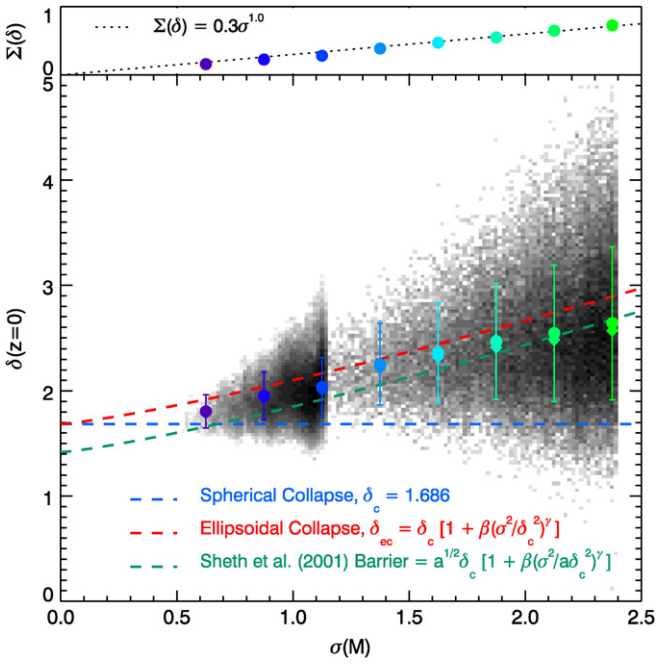

Figure 3. Smoothed linear overdensity δ, extrapolated to $z = 0$, as a function of smoothing scale $\sigma(M)$ for regions that collapse to form halos by $z = 0$. The circles correspond to the mean overdensities and the diamonds show the median overdensities, while the errorbars indicate the halo-to-halo scatter. The error on the mean is significantly smaller than the scatter in all cases. Shown for comparison are the spherical collapse barrier (δ_c, blue dashed line), the Sheth et al. (2001) ellipsoidal collapse barrier (δ_{ec}, red dashed line), and the collapse barrier associated with the Sheth & Tormen (1999) mass function (green dashed line). The upper panel shows the variation in the scatter of barrier heights, where he have used the Greek letter "Σ" to denote this scatter (not to be confused with $\sigma(M)$).

(A color version of this figure is available in the online journal.)

4. EXCURSION SET FIRST-CROSSING DISTRIBUTIONS AND MASS FUNCTIONS IN COSMOLOGICAL SIMULATIONS

The results presented in the previous section indicate that the linearly extrapolated overdensities of regions that collapse in cosmological simulations behave in a manner analogous to the expectations of the ellipsoidal collapse model. In this section, we test the second ingredient of the excursion set ansatz: the calculation of the first-crossing distribution and associated halo mass function with a particular barrier.

Tinker et al. (2008) used a large suite of cosmological simulations to determine an accurate numerical fit to the abundance of dark matter halos as a function of their mass. They found that the first-crossing distribution that corresponds to the halo mass function measured in simulations can be well described by the function

$$\nu_c f_T(\nu_c) = A_T \left[\left(\frac{e_T \nu_c}{\delta_c} \right)^{d_T} + \left(\frac{\nu_c}{\delta_c} \right)^{g_T} \right] \exp\left(-\frac{h_T \nu_c^2}{\delta_c^2} \right). \quad (23)$$

[6] Although this is not entirely self-consistent (the smoothing scale is related to the mass scale by $M \propto (1 + \delta)R^3$), it is clear that the error is small if this calculation is done at an epoch when δ is very small. We have tested that the epoch we use $a = 0.01$ is sufficiently early for this purpose.

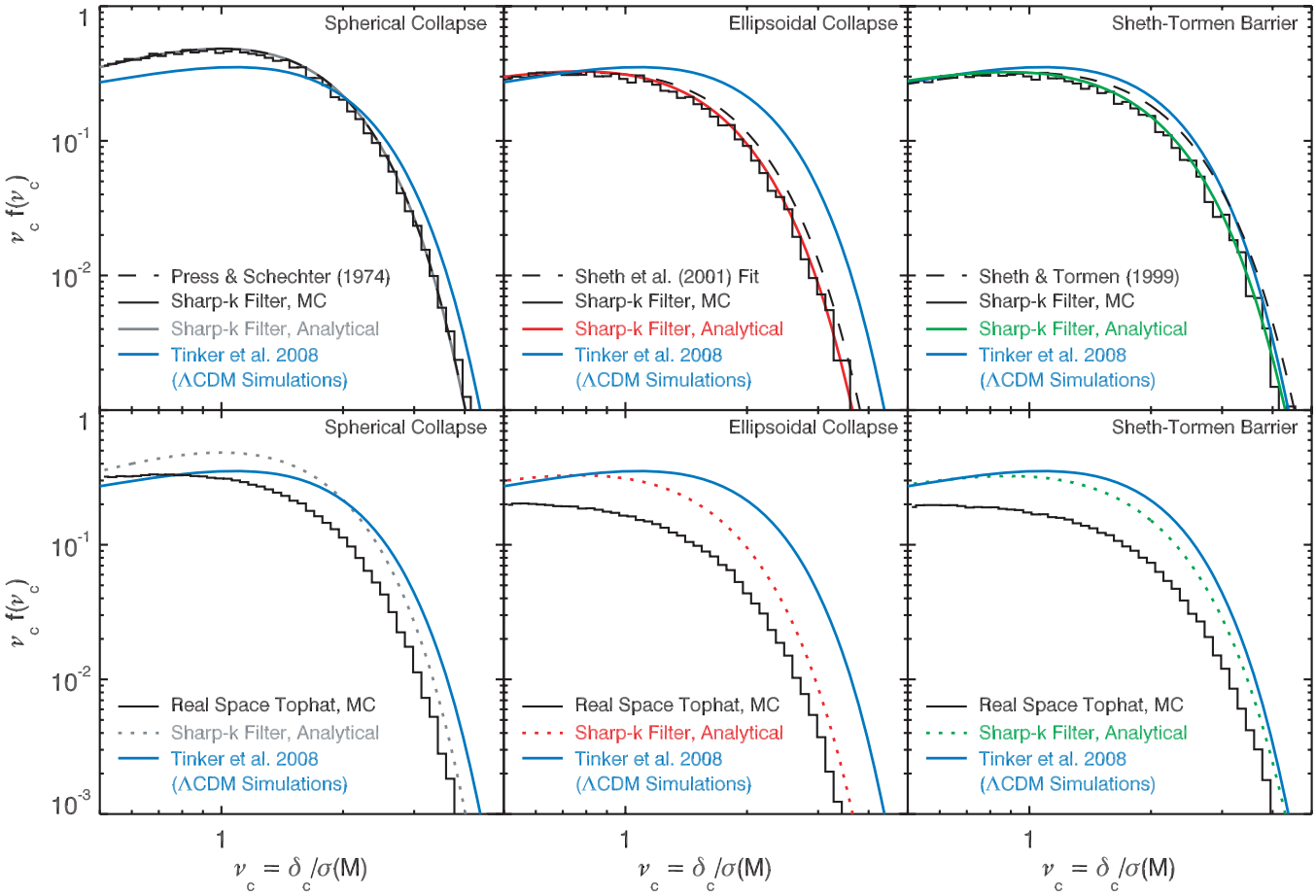

Figure 4. First-crossing distributions for common collapse barriers from the literature. The upper row shows distributions calculated with the sharp k-space top-hat filter for the spherical collapse barrier (Gunn & Gott 1972, gray line, upper left panel), the ellipsoidal collapse barrier (Sheth et al. 2001, red line, upper middle panel), and the collapse barrier associated with the Sheth & Tormen (1999) mass function (Sheth et al. 2001, green line, upper right panel). The colored lines indicate the sharp k-space excursion set first-crossing distributions calculated using the Zhang & Hui (2006) analytical method. The histograms indicate Monte Carlo realizations of the first-crossing distributions calculated by integrating the Langevin Equation (3). The dashed black lines indicate the analytical form for the Press & Schechter (1974) mass function (upper left panel), the Sheth et al. (2001) fit to the ellipsoidal collapse first-crossing distribution (upper middle panel), and the Sheth & Tormen (1999) mass function (upper right panel). Also shown is the Tinker et al. (2008) mass function determined from a large suite of cosmological simulations (blue line, all panels). In all cases, the Monte Carlo and Zhang & Hui (2006) first-crossing distributions agree well. Since the ellipsoidal collapse barrier lies above the spherical collapse barrier (see Figure 1), the corresponding first-crossing distribution predicts fewer galaxy mass ($\nu_c \gtrsim 0.5$) halos than does the Press & Schechter (1974) formula. The Sheth & Tormen (1999) mass function produces more high-mass halos by lowering the associated collapse barrier below the spherical collapse barrier $B_{\rm sc} = \delta_c$ at small $\sigma(M)$ (see Figure 1). For comparison, the bottom row shows the first-crossing distributions for the same barriers calculated using a real-space top-hat filter (histograms, bottom row). In each case, using a real-space top-hat filter produces fewer halos in the excursion set calculation than does the sharp k-space top hat for most halo masses.

(A color version of this figure is available in the online journal.)

For $\Delta = 200$ spherical overdensity halos, the best-fit mass function parameters are $A_T = 0.482$, $d_T = 1.97$, $e_T = 1$, $g_T = 0.51$, and $h_T = 1.228$ (with $\chi^2/\nu = 1.14$, see table C4 of Tinker et al. 2008).

Figure 4 compares the first-crossing distribution given by Equation (23) with first-crossing distributions calculated from the excursion set formalism with the collapse barriers described in Section 2. Where possible (i.e., in the case of sharp k-space top-hat window function) we have checked our Monte Carlo calculation of the first-crossing distribution against the direct solution of the Volterra equation using the method of Zhang & Hui (2006; see Appendix C) and have found excellent agreement.

The spherical collapse model (left column), corresponding to the Press & Schechter (1974) mass function, displays the well-known deficit of massive halos and overabundance of low-mass halos compared with simulations (see the discussion in Section 2.2 and Appendix A). As demonstrated first by Bond et al. (1991, see their Figure 5), changing the window function from the sharp k-filter to a real-space top-hat filter acts to reduce the abundance of galaxy-mass halos rather than improve the agreement between the spherical collapse and simulation first-crossing distributions.

Using the ellipsoidal collapse barrier presented by SMT01 (see Equation (18)) with the excursion set calculation results in a lower first-crossing distribution at galaxy masses (Figure 4, middle column) compared to the spherical collapse model. These first-crossing distributions lie slightly below the SMT01 fitting function (Equation (19)), and well below the Tinker et al. (2008) simulation results for $\nu_c > 1$. The ellipsoidal collapse barrier converges to the spherical collapse barrier as $\sigma(M) \rightarrow 0$, but at the mass scales probed in simulations [$\sigma(M) \gtrsim 0.5, M \lesssim 10^{15} h^{-1} M_\odot$] the ellipsoidal collapse barrier is considerably larger ($\delta_{\rm ec} \gtrsim 1.8$). The larger barrier height tends to suppress the abundance of halos in this mass range as calculated by the excursion set formalism. Similar results

have been obtained by other authors (e.g., Sandvik et al. 2007, their Figure 3), but the convergence to the spherical collapse model at $\nu_c >> 1$ is seldom commented upon. For consistency between the treatments of spherical and ellipsoidal collapse, the abundance of halos calculated for small ellipticities and prolaticities (i.e., at large masses) must be the same in both models. As with the spherical collapse model, the ellipsoidal collapse excursion set mass function calculated with a real-space top-hat filter acts to lower the abundance of galaxy-mass halos (Figure, 4, bottom, middle panel).

The Sheth et al. barrier (Equation (20)), which SMT01 presented as the barrier corresponding to the GIF simulation (ST99) mass function, produces a first-crossing distribution that lies below the Tinker et al. (2008) simulation results (Figure 4, right column). Note also that the predicted distribution does not agree with the SMT01 first-crossing distribution (Equation (21), dashed line, Figure 4, upper right panel), which this barrier is designed to describe. The relative disagreement between the Tinker et al. (2008) and SMT01 first-crossing distributions should be noted. This disagreement, although relatively small on the scale of this figure, is significant in terms of the halo abundance (see Tinker et al. 2008). For the first-crossing distribution determined using a real-space top-hat window function (Figure 4, lower right panel), the Monte Carlo calculation lies below the sharp k-space window function results and is discrepant with the simulation result.

Since all simulated mass functions are limited by their particle resolution one might wonder if the differences with the simulations owe to the differences in normalization, as all of the excursion set first-crossing distributions are normalized such that $\int f(\nu_c)d\nu_c = 1$. The form of the Tinker et al. (2008) first-crossing distribution (Equation (23)) that is plotted in Figure 4 is constructed to require that $\int f_T(\nu_c)d\nu_c = 1$. However, the free parameters of this function are fitted in a regime that incorporates only ≈60% of the available mass. To address this question, Figure 5 shows the ellipsoidal collapse first-crossing distribution normalized at a fixed mass scale (instead of the integral constraint) to match the Tinker et al. (2008) first-crossing distribution at large masses ($\nu_c = 3$), or constrained to provide the same integral over the same mass range (at $\nu_c \geqslant 3$). The functions clearly differ in shape and not simply in normalization.

Of the three barriers we examined, the excursion set first-crossing distributions calculated from the Sheth et al. barrier most closely approximate the Tinker et al. (2008) simulation results. This result is not surprising, given that the ST99 function is itself a fit to cosmological simulations. The ellipsoidal collapse barrier produces a first-crossing distribution that differs substantially from the ST99 fitting function, even though this mass function is frequently associated with ellipsoidal collapse model.

The results presented in this section demonstrate that *excursion set predictions disagree with* ΛCDM *simulation mass function results for all of these barriers.* Given that the overdensities of the collapsed regions behave similarly to the barrier shape expected for the ellipsoidal collapse, our results imply a manifest failure of the excursion set ansatz as a method of computing the abundance of collapsed objects. In Appendix D, we show that our results hold for other halo definitions, including FOF halos and other spherical overdensity definitions.

5. DISCUSSION

In the excursion set theory, the abundance, formation time, and bias of dark matter halos are assumed to be directly linked to the initial linear overdensity field extrapolated to a given epoch using linear growth rates. This assumption significantly simplifies modeling, but clearly needs to be tested against direct numerical simulations. Our results show that the linear overdensities around the Lagrangian positions of the centers of mass of collapsed halos in simulations behave in a manner analogous to the collapse overdensity barrier predicted by SMT01 using an ellipsoidal collapse model. The similar behavior suggests that this model captures the main physics behind the nonlinear gravitational collapse around peaks in the initial density field.

At the same time, the failure of the excursion set ansatz to predict correct abundance of collapsed halos with the ellipsoidal collapse barrier demonstrates that the ansatz is flawed. Several aspects of the ansatz may be responsible for its failure to accurately describe simulation results. For example, assumption that each mass element can be assigned to a collapsed halo using only the local overdensity independently of its environment is definitely problematic. The threshold overdensity for collapse (the barrier) in either the spherical or ellipsoidal collapse models is predicted for the volumes centered on a density peak, and not for a random mass element in the field. While the actual collapse will occur around the density peaks, additional mass near a peak may collapse onto it even though the extended region may not satisfy the local collapse condition. Our study highlights the failure of the excursion set ansatz on a statistical basis for the entire halo population, but a physical model for the collapse and formation of dark matter halos must also succeed object by

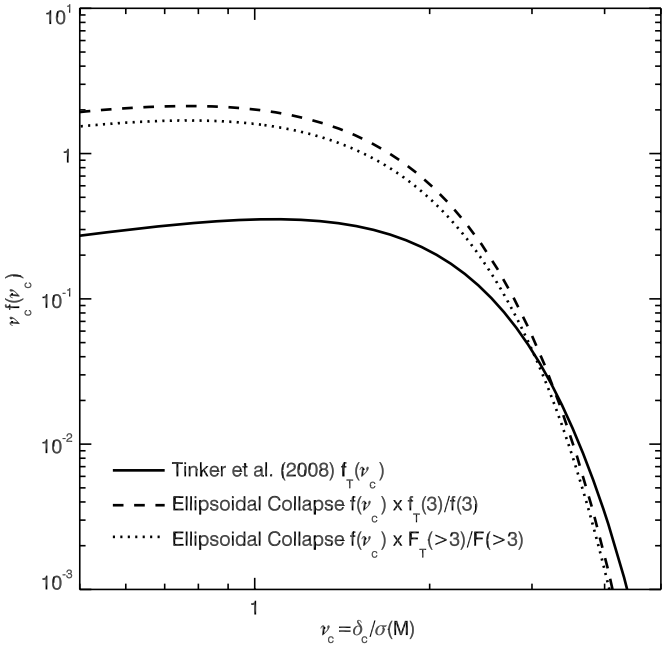

Figure 5. Renormalized first-crossing distributions for ellipsoidal collapse vs. the Tinker et al. (2008) simulation results. The form of the Tinker et al. (2008) mass function is normalized such that $\int f_T(\nu_c)d\nu_c = 1$, but the simulation results only probe masses $\nu_c \gtrsim 0.5$ that contain roughly 60% the mass of the universe. This figure demonstrates that any associated uncertainty with the normalization of the Tinker et al. (2008) mass function (solid line) cannot reconcile the difference with the ellipsoidal collapse first-crossing distribution. If the ellipsoidal collapse barrier (Equation (18)) first-crossing distribution is renormalized to match the Tinker et al. (2008) mass function at $\nu_c = 3$ (dashed line), or renormalized to match the integral of the Tinker et al. (2008) mass function at $\nu_c > 3$ (dotted line), the resulting distribution is still discrepant from the Tinker et al. (2008) results. Hence, the shape and normalization of the ellipsoidal collapse barrier excursion set mass function differs from the halo mass function determined by N-body cosmological simulations.

object (see, e.g., Katz et al. 1993). The methods for calculating the abundance of halos that treat individual peaks in the density field (Bond & Myers 1996; Monaco et al. 2002; N. Dalal et al. 2009, in preparation) may therefore afford a better way to predict the formation, masses, and abundances of collapsed objects.

The shape of the effective collapse barrier is determined both by the distribution of overdensities in a smoothed Gaussian field (e.g., with ellipticities and prolaticities, or other properties, sufficient for collapse) and by the dependence of the collapse condition on the overdensity (and/or other properties). The halo formation time can be defined relative to the mean assembly history (e.g., Wechsler et al. 2002), but the specific choice of definition can influence the relation between formation time and halo mass (for a recent discussion, see Li et al. 2008). In terms of the linear overdensity and the effective barrier B, one definition of halo collapse is simply that of Equation (12). Of course, determining the effective barrier B or measuring the collapse epoch z_c complicates the matter. The definition of collapse can be connected to the physical properties of halos through dynamical models, but identifying evolutionary phases in such simple models with the actual nonlinear growth of dark matter halos may be incorrect or inaccurate. For instance, the ellipsoidal collapse model of Bond & Myers (1996) associates halo formation with the collapse of the longest ellipsoid axis, while freezing the collapse of the shorter axis at a particular point to prevent a density singularity. Halo virialization, however, may be associated with the collapse of another axis or conditional properties of shape of the density or shear fields (e.g., Lee & Shandarin 1998; Monaco et al. 2002). These issues warrant a more careful examination that we defer for future work now that we have a statement of the problems at hand.

Dark matter halos reside in special locations of the density field, and have different clustering properties than bulk matter (e.g., Kaiser 1984; Efstathiou et al. 1988). Models of halo bias are tightly connected with the effective collapse barrier. Mo & White (1996) presented the idea that the biasing of halos is connected to the rate at which density trajectories cross two separate barriers, and used this concept to calculate the Lagrangian bias of halos in the Press–Schechter model. SMT01 adapted these ideas to calculate the halo bias implied by their modified ellipsoidal collapse model.

In principle, the same collapse barrier should predict consistently both the bias and mass function of halos. However, while the ST99 mass function models the halo abundance reasonably well, Seljak & Warren (2004) found that the SMT01 bias model does not work well at low masses. For massive halos at high ν_c, Cohn & White (2008) found that the Mo & White (1996) bias scaling works better than the SMT01 model (however, see Hu & Kravtsov 2003). Interestingly, Reed et al. (2009) found that early-forming halos in their simulations were well modeled by SMT01 at peak heights as large as $\nu_c \sim 4$ (at small ν_c, the large-scale bias they measure drops below the SMT01 model, in a manner similar to that found by Seljak & Warren 2004). We note that if the effective collapse barrier converges to the spherical collapse overdensity δ_c for large mass or highly biased halos, then one might expect the halo bias to mimic the Mo & White (1996) scaling at large ν_c. We speculate that the intriguing deviations between the models for halo bias and abundance of halos are connected to the current discrepancy between the effective collapse barrier and the abundance of halos in the excursion set ansatz that we discuss in this paper.

Lastly, the effective collapse barrier may be connected with the assembly bias phenomenon where dark matter halo clustering correlates with formation time. Gao et al. (2005) found that low-mass halos ($M < M_\star$) that formed early were much more strongly clustered than late-forming halos of the same mass (see also Sheth & Tormen 2004; Harker et al. 2006). Wechsler et al. (2006) demonstrated that the sense of assembly bias reverses at high-mass ($M > M_\star$) such that late-forming halos were more strongly clustered than early-forming halos at fixed mass, and that these correlations are reflected in the relative bias of halos with different concentrations at fixed mass (see also Wetzel et al. 2007; Jing et al. 2007).

Zentner (2007) in his review showed that window functions that are local in real-space rather than Fourier space naturally result in early-forming halos that reside in underdense regions, as reported for high-mass halos ($M > M_\star$) in the simulations. The standard implementation of the excursion set formalism assumes that the process of nonlinear collapse can be encapsulated into the assignment of the collapse barrier. For high-mass halos, tidal influences and nonlinear interactions with nearby objects should be minimal because halos with masses significantly larger than $M_\star$ form from nearly spherical peaks and usually dominate their local environments. As a result, the excursion set assumption should be most valid for high-mass ($M \gg M_\star$) halos and leads to a natural picture where early-forming, high-mass halos become less strongly clustered than their late-forming counterparts.

The reversal of the environment-dependent halo formation trend at low mass may owe to the truncation of small halo growth by nearby structure as suggested by Wang et al. (2007). Dalal et al. (2008) greatly extended this work, validating the high-mass trend in a set of scale-free numerical simulations and showing that environmental influences on halo bias, concentration, and formation time at fixed mass could be accounted for by considering the "peak curvature," $d\delta_{R_W}/d\sigma$, in addition to peak height. The peak curvature serves as some proxy for environment as peaks with greater curvature lie in relatively underdense environments. Dalal et al. (2008) also used a toy model to demonstrate that at small masses environmental effects, such as those suggested by Wang et al. (2007), can truncate halo growth and drive early-forming halos to become less anti-biased as they are advected by the larger-scale matter field.

Our results relate to these findings by providing a new outlook on the connection between halo abundance, the effective collapse barrier, and the excursion set formalism. If the excursion set formalism fails to account properly for the abundance of halos using an appropriate form for the collapse barrier, then it may also fail to describe reliably the connection between formation time, mass, and properties of the density field. The effective collapse barrier may well be a function of additional parameters beyond the local density (e.g., Chiueh & Lee 2001; Sandvik et al. 2007), may incorporate information about the larger-scale field (e.g., Zentner 2007; Desjacques 2008; Dalal et al. 2008), and may require additional parameter dependencies that to account for the nonlinear collapse of overdensities (e.g., Wang et al. 2007; Dalal et al. 2008).

At present, the excursion set theory provides the main framework used to develop heuristic understanding of simulation results and to formulate fits to simulation results for halo abundance, clustering, and other halo properties. The method succeeds in a gross sense. Excursion set theory identifies the fundamental scale in the problem, the mass where $\sigma(M) \sim \delta_c$. Below this characteristic mass the halo abundance per unit mass has a simple, power-law form, while above this mass the halo abundance drops rapidly. However, a precise understanding of halo

abundance and clustering beyond the gross accuracy provided by the excursion set ansatz is now necessary. Contemporary and forthcoming efforts to use measurements of the abundance and clustering of galaxy clusters to constrain cosmological parameters, as well as comprehensive statistical studies of galaxy formation and evolution, only highlight the need for a sound understanding of halo abundance and assembly, both globally and as a function of environment. We need to explore amendments and alternatives to the excursion set model to make progress in our understanding of halo formation.

6. SUMMARY

In this paper we have presented tests of the excursion set ansatz against cosmological simulations. Using a subset of cosmological simulations from the Tinker et al. (2008) study of the halo mass function, we identify the locations in the linear overdensity field that later collapse to form dark matter halos. We demonstrate that the dependence of the linear overdensity of these regions on mass or smoothing scale $\sigma(M)$ resembles predictions of the ellipsoidal collapse model. While the effective collapse barrier of simulated halos behaves analogously to the simple ellipsoidal collapse barrier, the simulated halo mass function is inconsistent with what the excursion set ansatz predicts for such a barrier. This inconsistency implies that the excursion set ansatz is not valid and cannot be used reliably to predict halo abundance or bias.

The modified collapse barrier of Sheth et al. (2001) differs significantly from the physical behavior calculated by the ellipsoidal collapse model, which for example predicts convergence to the spherical barrier ($\delta \to \delta_c$) for the rarest peaks ($\sigma \to 0$). In view of this, the interpretation of the Sheth & Tormen (1999) mass function as a prediction of the ellipsoidal collapse model for the abundance of dark matter halos is not correct.

The impressive statistics of ever-larger dark matter simulations will likely continue to uncover increasingly subtle variations on the classical picture of dark matter halo formation. In this work, we identify a striking inconsistency between the effective collapse barrier of simulated halos and excursion set formalism predictions for their abundance. Our results also demonstrate that there is still much to learn and understand about the conditions for and the process of halo collapse, which warrants further studies that critically revisit these issues using modern large cosmological simulations.

We thank Anatoly Klypin for access to his cosmological simulations and Neal Dalal for useful discussions on the subject of this study. BER gratefully acknowledges support from a Spitzer Fellowship through a NASA grant administrated by the Spitzer Science Center. A.V.K. is supported by the NSF under grants AST-0239759 and AST-0507666 and by NASA through grant NAG5-13274. B.E.R. and A.V.K. are also partially supported by the Kavli Institute for Cosmological Physics at the University of Chicago. A.R.Z. is supported by the University of Pittsburgh and by the NSF through grant AST 0806367. A.R.Z. would like to thank the Michigan Center for Theoretical Physics at the University of Michigan for support and hospitality while some of this work was being performed. Some of the calculations used in this work have been performed on the Joint Fermilab-KICP Supercomputing Cluster, supported by grants from Fermilab, the Kavli Institute for Cosmological Physics, and the University of Chicago. One of the simulations was performed at the Leibniz Rechenzentrum Munich, partly using German Grid infrastructure provided by AstroGrid-D.

APPENDIX A

SPHERICAL COLLAPSE

A simple approximation for the dynamical evolution of an overdense region is the spherical collapse model. The dynamical equation for the expansion and collapse of a spherical overdensity Δ of physical size $R_{\rm phys}(z)$ in a flat universe with a cosmological constant can be written (e.g., Gunn & Gott 1972)

$$\frac{d^2 a_R}{dt^2} = \frac{8}{3}\pi G \bar{\rho}_\Lambda a_R - \frac{4}{3}\pi G \bar{\rho}_m a_R[1 + \Delta(t)], \tag{A1}$$

where $a_R = R_{\rm phys}/R$ is the scale factor of the region, $\bar{\rho}_\Lambda = \Omega_\Lambda \rho_c$ is the dark energy density, and Ω_Λ is the dark energy density parameter. The corresponding growing *linear* overdensity δ obeys the differential equation

$$\frac{d^2\delta}{dt^2} + 2H\frac{d\delta}{dt} = 4\pi G \bar{\rho}_m \delta \tag{A2}$$

(e.g., Lifshitz 1946; Peebles 1965), while the physical overdensity evolves as

$$\Delta(t) = \frac{a^3}{a_R^3} - 1, \tag{A3}$$

where a is the universal scale factor. The initial conditions for evolving Equation (A1) are simply

$$a_R(t_{\rm init}) = a(t_{\rm init})(1 - \delta(t_{\rm init})/3), \tag{A4}$$

$$\dot{a_R}(t_{\rm init}) = H(t_{\rm init})a_R(t_{\rm init}) - a(t_{\rm init})H_D(t_{\rm init})\delta/3, \tag{A5}$$

where $H_D = \dot{D}/D$ describes the rate of change of overdensities. Initially $\Delta(t) \simeq \delta(t)$, as can be checked by Taylor-expanding Equation (A3) and comparing it with Equation (A4), but eventually the quantities diverge as the overdensity begins to exceed the applicability of the linear order approximation. As the spherical region begins to break from the universal expansion and reaches a maximum radius at the turn-around time $t = t_{\rm ta}$, the physical overdensity reaches $1 + \Delta(t = t_{\rm ta}) \simeq 5.55$ while the linear overdensity is $\delta(t = t_{\rm ta}) \simeq 1.06$. As the region collapses to a point of zero size, $\Delta \to \infty$ while the linearly extrapolated overdensity approaches a value of

$$B_{\rm sc} \equiv \delta_{\rm sc} = \delta(t_{\rm init})D(z_c)/D(z_{\rm init}) = \delta_c \quad \text{(SphericalCollapse)}, \tag{A6}$$

where $\delta_c = 1.686$ is often called the linear collapse overdensity for the growth of spherical perturbations (Gunn & Gott 1972; Peebles 1980) for an $\Omega_m = 1$ universe (δ_c has a weak dependence on cosmology; see, e.g., Bond & Myers 1996; Eke et al. 1996). If the spherical collapse of the region to zero size is associated with the formation of a dark matter halo, then Equation (A6) can be used as the "spherical collapse barrier" for purposes of calculating the first-crossing distribution associated with spherical collapse.

APPENDIX B

ELLIPSOIDAL COLLAPSE AND ITS MODIFICATIONS

The gravitational collapse calculation has been generalized to model nonspherical collapse by a number of authors (e.g., Zel'dovich 1970; Nariai & Fujimoto 1972; Hoffman 1986; Bertschinger & Jain 1994; Eisenstein & Loeb 1995; Bond &

Myers 1996; Audit et al. 1997; Del Popolo et al. 2001; Shen et al. 2006). Below we focus on an ellipsoidal collapse model by Bond & Myers (1996, see their Section 2.1.3 and Appendix A), which treats the gravitational collapse of a homogeneous ellipsoid by separately following the coupled evolution of each axis a_i of the ellipsoid. Bond & Myers (1996) showed that the dynamical equation for the expansion and collapse of an ellipsoidal region with linear overdensity $\delta(t = t_{\rm init}) = \delta_0$ at an initial time $t_{\rm init}$ can be written

$$\frac{d^2a_i}{dt^2} = \frac{8}{3}\pi G\bar{\rho}_\Lambda a_i - 4\pi G\bar{\rho}_m a_i\left[\frac{1}{3} + \frac{\Delta(t)}{3} + \frac{b_i'(t)}{2}\Delta(t) + \lambda_i'(t)\right] \quad \text{(B1)}$$

where the index $i = 1, 2, 3$ indicates a principal axis. The term

$$b_i' = -\frac{2}{3} + a_1a_2a_3\int_0^\infty \frac{d\tau}{\left(a_i^2+\tau\right)\Pi_{m=1}^3\left(a_m^2+\tau\right)^{1/2}} \quad \text{(B2)}$$

describes triaxial contributions to the gravitational acceleration. A linear order approximation of the effects of external tides on the evolution of the region are included through the factors $\lambda_i'(t) = \lambda_i - \delta/3$, which are written in terms of the eigenvalues of the strain tensor

$$\lambda_3 = \frac{\delta}{3}(1 + 3e + p), \quad \text{(B3)}$$

$$\lambda_2 = \frac{\delta}{3}(1 - 2p), \quad \text{(B4)}$$

$$\lambda_1 = \frac{\delta}{3}(1 - 3e + p). \quad \text{(B5)}$$

Here, $e \geqslant 0$ is the ellipticity, $-e \leqslant p \leqslant e$ is the prolaticity, and the eigenvalues are ordered $\lambda_3 \geqslant \lambda_2 \geqslant \lambda_1$. This linear order approximation to the effects of tides grows as $\lambda_i(t) \propto \delta(t) \propto D(t)$. The physical overdensity in the ellipsoidal collapse model evolves simply as

$$\Delta(t) = \frac{a^3}{a_1a_2a_3} - 1, \quad \text{(B6)}$$

where a is the universal scale factor. The initial conditions for evolving Equation (B1) are

$$a_i(t_{\rm init}) = a(t_{\rm init})[1 - \lambda_i(t_{\rm init})], \quad \text{(B7)}$$

$$\dot{a}_i(t_{\rm init}) = H(t_{\rm init})a_i(t_{\rm init}) - a(t_{\rm init})H_D(t_{\rm init})\lambda_i(t_{\rm init}), \quad \text{(B8)}$$

The evolution of the region is then determined by the cosmology, the initial overdensity δ_0, the ellipticity e, the prolaticity p, and the initial universal scale factor $\bar{a}(t = t_{\rm init})$. For a spherical system ($e = 0$, $p = 0$, $a_1 = a_2 = a_3$), the dynamical equations reduce to Equation (A1).

Sheth et al. (2001) used the results of Doroshkevich (1970) to show that, in the context of the Bond & Myers (1996) ellipsoidal collapse model, the formula

$$g(e, p|\delta) = \frac{1125}{\sqrt{10\pi}}e(e^2 - p^2)\left(\frac{\delta}{\sigma}\right)^5 \exp\left[-\frac{5}{2}\frac{\delta^2}{\sigma^2}(3e^2 + p^2)\right] \quad \text{(B9)}$$

provides the expected distribution of ellipticities and prolaticities for the shear field of Gaussian random overdensities and corresponds to a distribution of effective collapse barriers for halos (as a function of e and p) that describes the overdensity at which the last (longest) principal axis collapses. Sheth et al. (2001) provided an empirically determined, implicit functional form to approximate the shape of the ellipsoidal collapse barrier in terms of e and p,

$$\frac{\delta_{\rm ec}(e, p)}{\delta_{\rm sc}} = 1 + \beta\left[5(e^2 \pm p^2)\frac{\delta_{\rm ec}^2(e, p)}{\delta_{\rm sc}^2}\right]^\gamma, \quad \text{(B10)}$$

which follows the most probable ($p = 0$) trend of the collapse barrier distribution well for the parameter values $\beta = 0.47$ and $\gamma = 0.615$ (a more recent calculation has found $\beta = 0.412$ and $\gamma = 0.618$, Desjacques 2008). For the most probable prolaticity $p = 0$, the maximum of the probability distribution $g(e, p = 0|\delta)$ follows the ridgeline $e_{\rm mp} = (\sigma/\delta)\sqrt{5}$. Substituting $p = 0$ and $e = e_{\rm mp}$ into Equation (B10) yields a characteristic ellipsoidal collapse barrier in terms of the overdensity variance as

$$B_{\rm ec} \equiv \delta_{\rm ec} = \delta_{\rm sc}\left[1 + \beta\left(\frac{\sigma^2}{\delta_{\rm sc}^2}\right)^\gamma\right]. \quad \text{(B11)}$$

Note that this barrier reduces to the spherical collapse barrier [$B = \delta_c$, Equation (15)] for large halo masses (small variances). For reference, the ellipsoidal collapse barrier is plotted in Figure 1 with the Sheth et al. (2001) parameters (dashed red line).

APPENDIX C

AN INTEGRAL METHOD FOR FIRST-CROSSING DISTRIBUTIONS WITH SHARP k-SPACE FILTERING

Typically, the first-crossing distribution is determined with a Monte Carlo approach (effectively by integrating Equation (3)). For the case of sharp k-space filtering, where smoothed overdensity executes a Markovian random walk with the smoothing scale, and barriers with a suitably weak dependence on the variance, Zhang & Hui (2006) showed that by properly accounting for the rate of first barrier crossings in an ensemble of trajectories, an integral relation for the first-crossing distribution could be expressed in terms of the functional form of the barrier B and the probability $P(\delta, S)$ that a trajectory δ first crosses the barrier near S. Specifically, in terms of the barrier $B(S)$, the first-crossing distribution satisfies

$$1 = \int_0^S f(S')dS' + \int_{-\infty}^{B(S)} P(\delta, S)d\delta \quad \text{(sharp}-k\text{filtering)}. \quad \text{(C1)}$$

The first term on the right hand side accounts for trajectories that have crossed at scales larger than S, while the second term

$$P(\delta, S) = P_0(\delta, S) - \int_0^S dS' f(S')P_0(\delta - B(S'), S - S') \quad \text{(C2)}$$

subtracts the rate of down-crossings from the probability

$$P_0(\delta, S) = \frac{1}{\sqrt{2\pi S}}\exp\left(-\frac{\delta^2}{2S}\right) \quad \text{(C3)}$$

that a trajectory given crosses the barrier near S. Equation (C1) can be differentiated and combined with Equations C2-C3 to produce a Volterra integral equation of the second kind for the first-crossing distribution

$$f(S) = g_1(S) + \int_0^S f(S)g_2(S, S')dS' \quad \text{(sharp}-k\text{filtering)}, \quad \text{(C4)}$$

with

$$g_1(S) = \left[\frac{B(S)}{S} - 2\frac{dB}{dS}\right] P_0(B(S), S) \quad \text{(C5)}$$

$$g_2(S, S') = \left[2\frac{dB}{dS} - \frac{B(S) - B(S')}{S - S'}\right] P_0(B(S) - B(S'), S - S') \quad \text{(C6)}$$

Hence, given a barrier shape $B(S)$, Zhang & Hui (2006) have provided a helpful method for calculating the first-crossing distribution for a k-space filter via Equation (C4).

APPENDIX D

THE EXCURSION SET ANSATZ AND HALO MASS DEFINITIONS

The results of Section 3 demonstrate a disconnect between the characteristic linear overdensity of regions that collapse to form dark matter halos and the collapse barrier required to reproduce the abundance of those same halos using the excursion set formalism. While the results of Section 3 are internally consistent, one might wonder if the failure of the excursion set ansatz was peculiar to the $\Delta = 200$ spherical overdensity halo definition. In this Appendix, we demonstrate that the excursion set ansatz also fails for other common halo definitions (specifically, $\Delta = 100$ spherical overdensity halos, $\Delta = 600$ spherical overdensity halos, FOF halos, and halos defined by spherical regions of size $R = 2R_{200}$). Since these halo definitions span the most practical definitions found in the literature, the results of this appendix present an exhaustive study of how our results depend on the halo and mass definitions. Further, since the largest simulation we study has a 1 h^{-3} Gpc^3 volume, the linear overdensity of regions with very large mass ($M_{200} \gtrsim 5 \times 10^{15} h^{-1} M_\odot$) are not probed by our simulations. Below, using extrapolations of the $\delta - \sigma(M)$ trend for various halo mass definitions, we demonstrate that even if $\delta \not\to \delta_c$ as $\sigma(M) \to 0$ the excursion set mass functions do not reproduce the simulated mass function for any halo mass definition we consider.

To repeat the calculations in Section 3 for other halo definitions, we must construct additional halo catalogs. For the spherical overdensity halo definition, we follow Tinker et al. (2008) and define halos with an overdensity Δ relative to the background density $\bar{\rho}_m$ as the particles within a radius R_Δ around density peaks. For the FOF halo definition (e.g., Davis et al. 1985), we adopt the standard linking length of $b = 0.2$. For halos defined by spherical regions of size $R = 2R_\Delta$, we use the $\Delta = 200$ catalog to identify halos and redefine the halo masses by assigning all particles within $2R_{200}$ of the center-of-mass membership in the halo. If the radius $R = 2R_{200}$ for one halo includes the center of mass of a smaller halo, the smaller halo is discarded from the catalog.

For each halo definition, the mass function dn/dM is determined by constructing a histogram for the halos by binning in mass. The first-crossing distributions $f(\nu_c)$ corresponding to each mass function are calculated using Equation (14). For each mass bin we calculate jack-knife errors, as described in detail by Tinker et al. (2008). For two spherical overdensity definitions, $\Delta = 200$ and $\Delta = 600$, we simply adopt a mass function of the form of Equation (23) with the best-fit parameters determined in Appendix C of Tinker et al. (2008). For $\Delta = 200$, $A_T = 0.482$, $d_T = 1.97$, $e_T = 1$, $g_T = 0.51$, and $h_T = 1.228$. For $\Delta = 600$, $A_T = 0.494$, $d_T = 2.56$, $e_T = 0.93$, $g_T = 0.45$, and $h_T = 1.553$. These analytical mass function fits make use of the wide range of simulations studied by Tinker et al. (2008). For mass functions for the other halo definitions, we rely on our halo catalogs for the L1000W simulation and represent the mass function with binned values and uncertainty estimates constructed from these catalogs. We have checked that the first-crossing distribution calculated from the binned mass function for the $\Delta = 200$ and $\Delta = 600$ halos in the L1000W simulation match the corresponding analytical fits from Tinker et al. (2008) extremely well, and we therefore expect that the binned mass functions and first-crossing distributions for the other halo mass definitions are reliable estimates of the halo abundance over the mass range probed by the L1000W simulation. The L1000W simulation is sufficient for our needs, as the primary constraint comes from the most massive halos in our catalogs.

We construct the distribution of linear overdensity δ as a function of the smoothing scale $\sigma(M)$ for the regions that collapse to form halos in the manner described in Section 3.2, using the same set of smoothed linear density fields calculated in Section 3.1. The mean of the $\delta(\sigma)$ distribution is calculated in three bins of width $\Delta\sigma = 0.25$. For the $\Delta = 200$ halo definition, the calculation results in the distribution of δ versus $\sigma(M)$ shown in Figure 3 (at $\sigma(M) \lesssim 1.2$).

To calculate an excursion set mass function from the overdensity distribution for each halo mass definition, the mean overdensity δ as a function of $\sigma(M)$ is fit with two analytical forms to produce two model collapse barriers. We first fit the function

$$\delta_{\rm fit} = \delta_c \left[1 + \beta(\sigma^2/\delta_c^2)^\gamma\right], \quad \text{(D1)}$$

used by Sheth et al. (2001) to represent ellipsoidal collapse, allowing β and γ to vary. By construction, this function converges to $\delta_{\rm fit} \to \delta_c$ as $\sigma \to 0$. We also fit a linear function,

$$\delta_{\rm lin} = A\sigma + b, \quad \text{(D2)}$$

allowing A and b to vary. The intercept b in general is smaller than δ_c; this functional form thus allows us to test how results would change if the barrier does not asymptote to δ_c for low values of σ. The best-fit parameters for the effective collapse barrier for each halo mass definition are reported in Table 1. We then use the best-fit parameters for Equations D1 and D2 to calculate a sharp k-space first-crossing distribution via the method of Zhang & Hui (2006; i.e., Equation (C4)), and compare with the simulated first-crossing distribution provided by the halo catalog.

Figure 6 shows the distribution of linear overdensity δ with smoothing scale $\sigma(M)$ for the $\Delta = 200$ halo catalog. As in Figure 3, the mean overdensity of regions that collapse to form halos in the $\Delta = 200$ catalog lie above the spherical collapse barrier δ_c. Analytical fits to the mean of the overdensity distribution (i.e., the effective collapse barrier for this halo mass definition) show that a simple linear extrapolation possibly suggests that $\delta \to 1.5$ as $\sigma \to 0$. The excursion set first-crossing distributions calculated for models of the mean overdensity in regions that form $\Delta = 200$ halos show that the differences in the fits at $\sigma \lesssim 0.45$ have little influence on the resulting halo abundance, as the larger $\delta > \delta_c$ at scales $\sigma \gtrsim 0.45$ suppresses the abundance of halos at $\nu_c < 4$ relative to the spherical collapse or Tinker et al. (2008) $\Delta = 200$ mass functions (see the right panel of Figure 6).

Changing the overdensity threshold in the spherical overdensity halo definition has an intuitive effect on the linear overdensity of regions that collapse to form halos. A higher threshold overdensity, such as a $\Delta = 600$ halo mass definition (Figure 7),

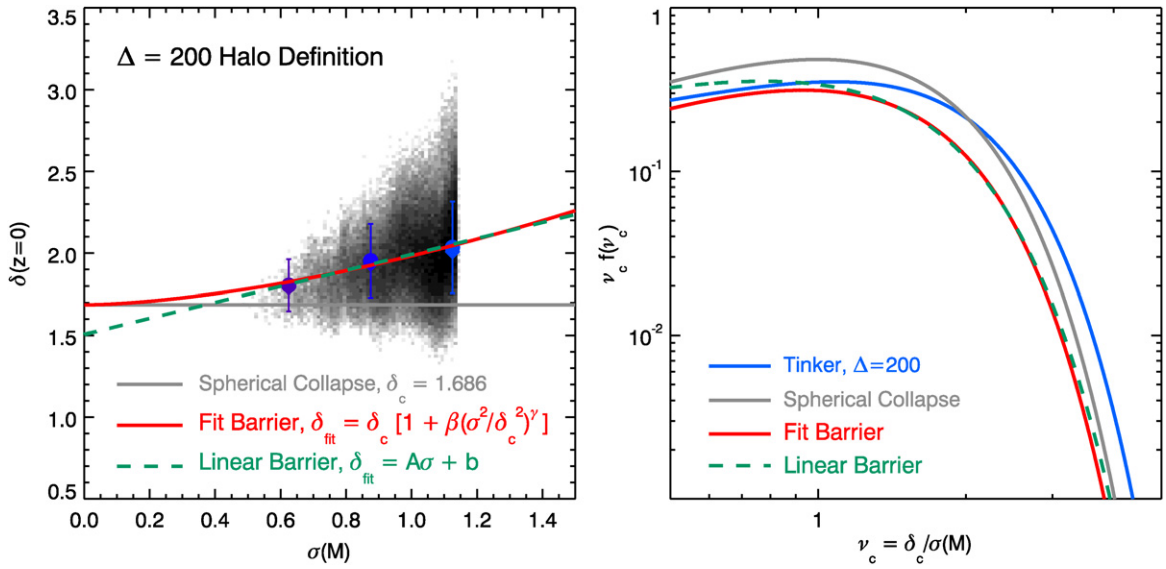

Figure 6. Smoothed linear overdensity δ, extrapolated to $z = 0$, as a function of smoothing scale $\sigma(M)$ for regions that collapse to form $\Delta = 200$ halos by the present epoch (left panel). The circles correspond to the mean overdensities, while the error bars indicate the halo-to-halo scatter. The error on the mean is significantly smaller than the scatter in all cases. Shown for comparison is the spherical collapse barrier (δ_c, solid gray line). Solid red line shows a fit of the functional form of the ellipsoidal collapse barrier to the simulation results, while the dashed green line shows a simple linear fit. The right panel shows excursion set mass functions for each model barrier calculated using the method of Zhang & Hui (2006) with sharp k filter and compared with the spherical collapse (gray line, right panel) and Tinker et al. (2008) $\Delta = 200$ (blue line, right panel) mass functions.

(A color version of this figure is available in the online journal.)

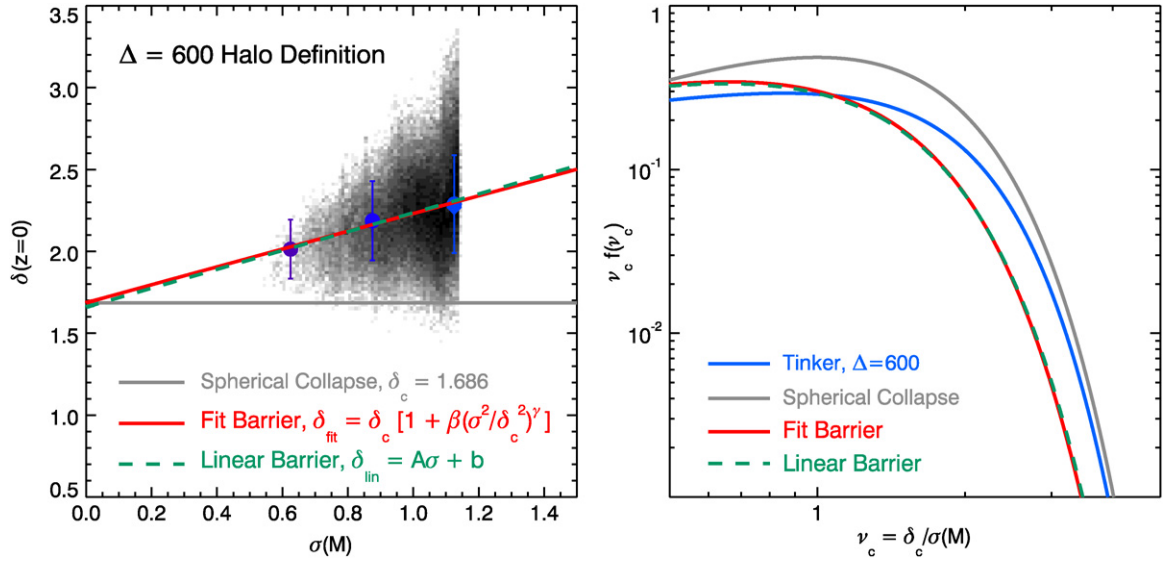

Figure 7. Same as for Figure 6, but for halos defined with a $\Delta = 600$ spherical overdensity criterion. Increasing the overdensity threshold in the halo mass definition does not improve the agreement between the excursion set and simulated halo mass function.

(A color version of this figure is available in the online journal.)

Table 1
Best-Fit Barrier Model Parameters

Mass Definition	β	γ	A	b
$\Delta = 100$	0.396	1.242	0.442	1.441
$\Delta = 200$	0.411	0.809	0.487	1.506
$\Delta = 600$	0.543	0.496	0.576	1.660
FOF	0.363	0.890	0.458	1.493
$R_{\rm vir} = 2R_{\Delta=200}$	···	···	0.409	1.348

results in a higher characteristic linear overdensity for regions that collapse to form halos. Model fits to the mean overdensity with smoothing scale show that the mean overdensity increases roughly linearly, and approaches $\delta \to \delta_c$ as $\sigma \to 0$. The abundance of halos is correspondingly suppressed, with the model barrier fits producing very similar excursion set first-crossing distributions that lie below the spherical collapse mass function. The simulated $\Delta = 600$ mass function from Tinker et al. (2008) has a lower abundance than the lower threshold $\Delta = 200$ mass function, but the excursion set mass functions are significantly lower than the simulated $\Delta = 600$ mass function (Figure 7, right panel). In this case, increasing the overdensity threshold does not improve the performance of the excursion set ansatz. Similarly, using a lower threshold such as a $\Delta = 100$ halo mass definition (Figure 8), does not bring the excursion set and simulated mass functions into agreement. The lower overdensity

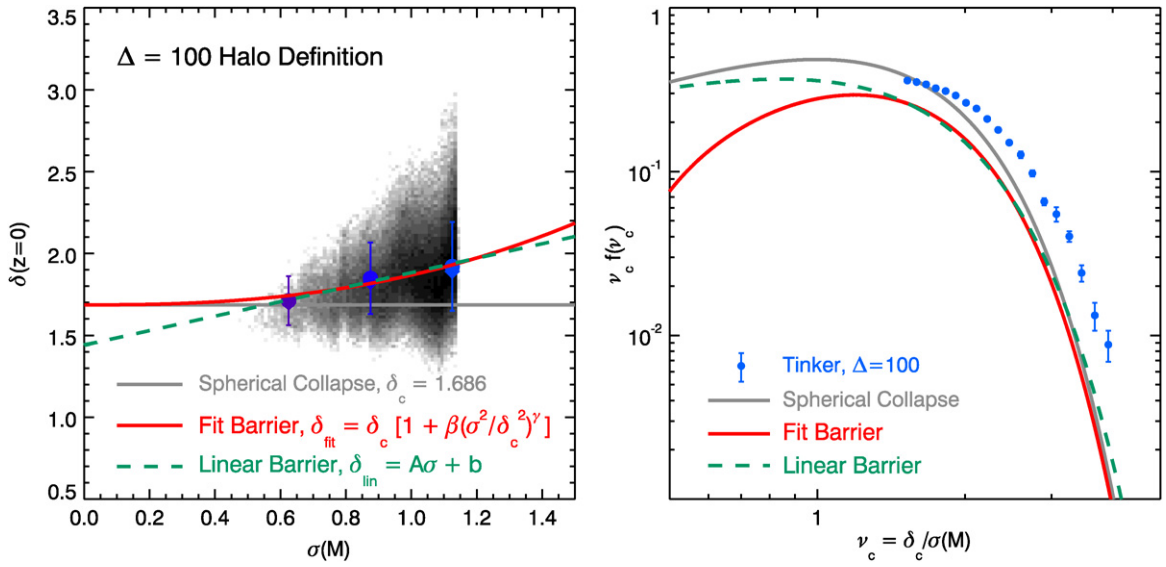

Figure 8. Same as for Figure 6, but for halos defined with a $\Delta = 100$ spherical overdensity criterion. Here, the simulated halo mass function is measured directly from only the L1000W simulation (points and error bars).

(A color version of this figure is available in the online journal.)

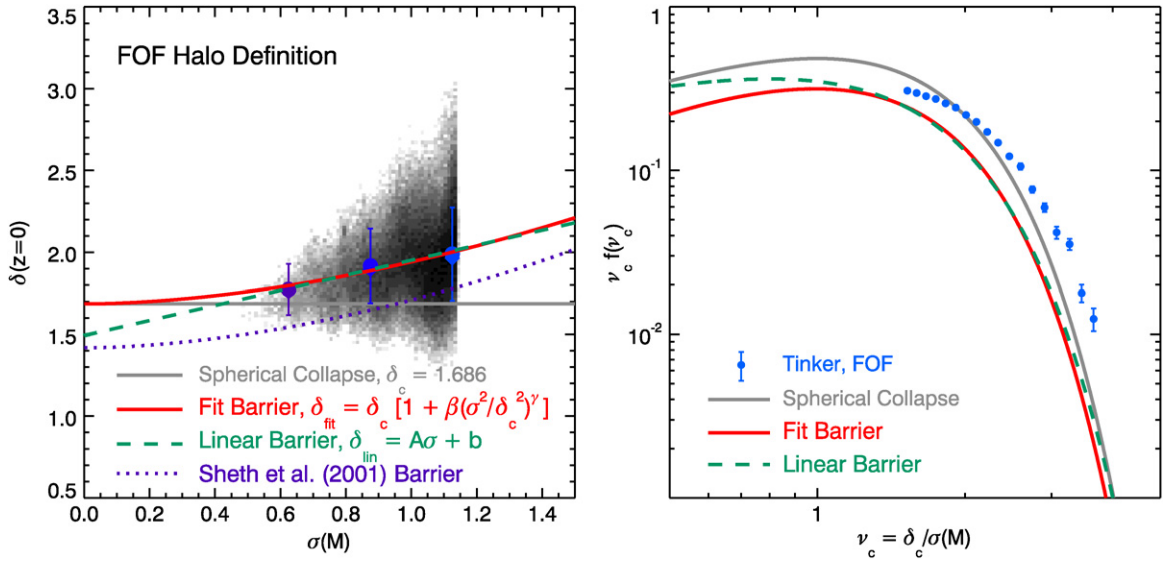

Figure 9. Same as for Figure 8, but for halos defined with a FOF algorithm using a linking length of $b = 0.2$. The characteristic linear overdensity of regions that collapse to form FOF halos does not follow the modified ellipsoidal collapse barrier presented by (Sheth et al. 2001, purple dotted line). Changing the halo definition from spherical overdensity to FOF halos does not improve the agreement between the excursion set and simulated halo mass function. The simulated halo mass function is measured directly from only the L1000W simulation (points and error bars).

(A color version of this figure is available in the online journal.)

threshold decreases the characteristic linear overdensity of regions that collapse to form halos and increases the abundance of regions that can collapse. However, the mean overdensity does not decrease significantly below the spherical collapse overdensity and the excursion set mass functions only begin to roughly match abundance predicted by the spherical collapse mass function. The simulated $\Delta = 100$ mass function has increased the abundance of halos relative to the $\Delta = 200$ mass function, so the disagreement between the excursion set mass function and the simulated mass function still remains for this lowered overdensity threshold (Figure 8, right panel).

Altering the mass definition from spherical overdensity to FOF halos does not improve the agreement between the simulated and excursion set mass function. The original motivation presented by Sheth et al. (2001) for modifying the ellipsoidal collapse barrier to the lower limiting value of $\delta_{\rm SMT} \rightarrow \sqrt{a_{\rm SMT}}\delta_c$ as $\sigma \rightarrow 0$ was the use of a FOF definition in identifying halos in the GIF simulation. Figure 9 demonstrates explicitly that the characteristic linear overdensity of regions that collapse to form FOF halos does not follow Equation 20; the mean overdensity is similar to that found for $\Delta = 200$ halos. Similarly, the excursion set mass functions calculated from the model fits to the mean overdensity of regions that collapse to form FOF halos do not match the simulated FOF halo mass function.

We could also redefine the mass from the $\Delta = 200$ halo definition to include all particles within a modified "virial" radius $R = 2R_{200}$. This halo mass definition is intended as an analogy to the "static" mass halo definition proposed by Cuesta

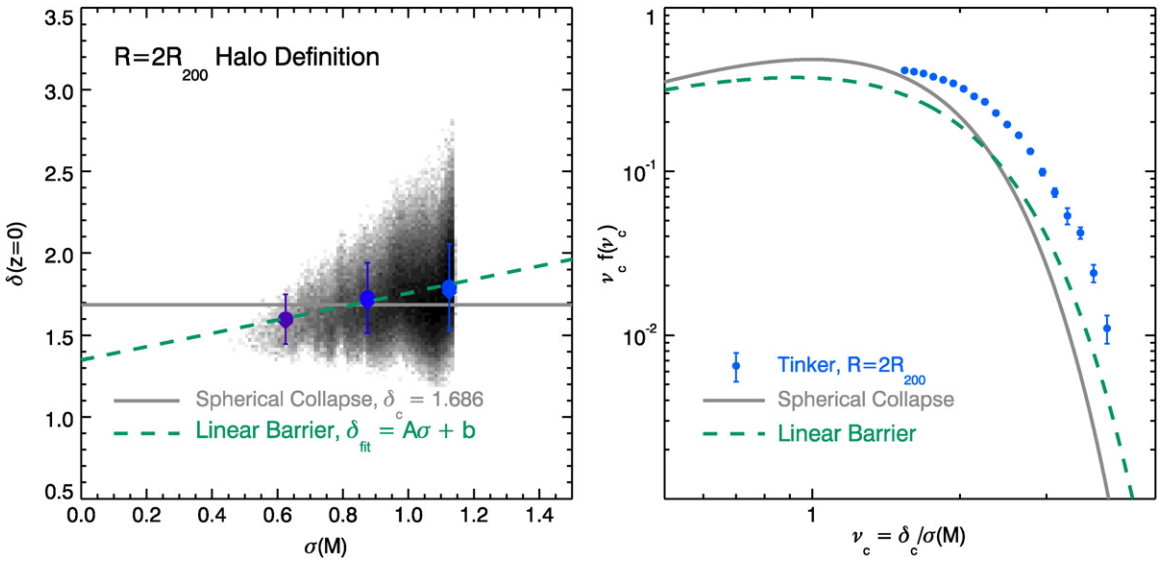

Figure 10. Same as for Figure 8, but for $\Delta = 200$ halos with masses rescaled to include all particles within a radius $R = 2R_{200}$. In this halo definition, small $\Delta = 200$ halos with centers of mass that reside within a distance R of larger halos are incorporated into the larger system. The mean of the linear overdensity distribution in this case lies below the spherical collapse barrier at small σ, so only the excursion set mass function for the linear barrier (which allows $\delta < \delta_c$) is compared with the simulated mass function (right panel). Changing the halo mass definition to increase the region incorporated into halos identified by a $\Delta = 200$ spherical overdensity criterion does not improve the agreement between the excursion set and simulated halo mass function (points and error bars).

(A color version of this figure is available in the online journal.)

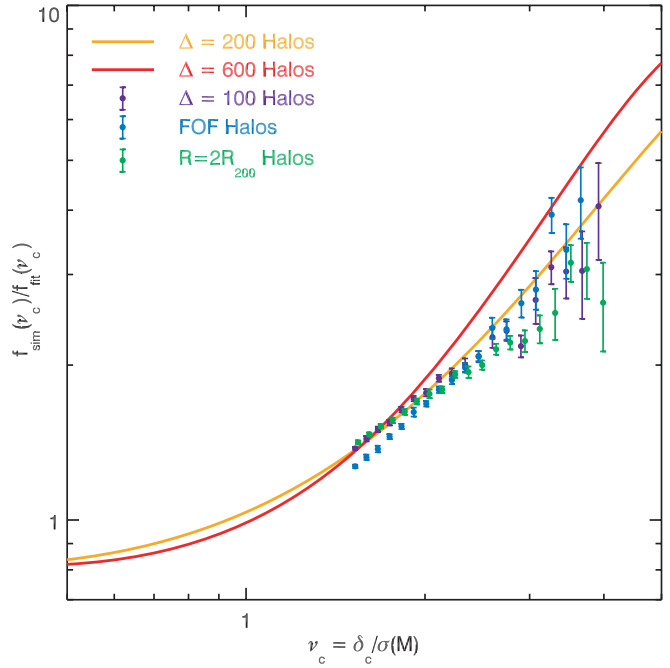

Figure 11. Ratio $f_{\rm sim}(\nu_c)/f_{\rm fi}(\nu_c)$ of the simulated first-crossing distribution $f_{\rm sim}$ to the excursion set first-crossing distribution $f_{\rm fit}$ calculated from a linear fit to the overdensity distribution plotted in Figures 6–10 for a variety of halo mass definitions, plotted as a function of peak height $\nu_c = \delta_c/\sigma(M)$. For the $\Delta = 200$ (orange line) and $\Delta = 600$ (red line) spherical overdensity halo definitions, the analytical fits from Tinker et al. (2008) are compared with the calculated first-crossing distributions. For $\Delta = 100$ spherical overdensity halos (purple points), FOF halos (blue points), and halos with masses defined by the particle content within a radius $R = 2R_{200}$ (green points), the binned first-crossing distributions from the L1000W simulation halo catalog were compared with the excursion set results at the appropriate ν_c for each mass bin. For these halo mass definitions, the uncertainty estimates in $f_{\rm sim}/f_{\rm fit}$ reflect the same fractional uncertainty in the simulated first-crossing distributions shown in Figures 8–10. For every halo mass definition, that $f_{\rm sim}/f_{\rm fit}$ is not constant with ν_c demonstrates that the disagreement between the simulated and excursion set first-crossing distributions differ in shape and not simply in relative normalization.

(A color version of this figure is available in the online journal.)

et al. (2008), who found that halos defined by regions with zero mean radial velocity (with a size of approximated $2 \times R_{\rm vir}$, see their Figure 14) displayed an abundance similar to the Press–Schechter spherical collapse mass function at $z = 0$. This halo definition results in halo abundance roughly twice that found by Cuesta et al. (2008) at fixed mass because the effective $R_{\rm vir}/R_{200}$ ratio is mass-dependent, but provides a useful example of a mass definition that incorporates very large regions into single halos. Figure 10 shows that the linear overdensity of regions that collapse to form halos defined in this manner is typically low, since the typical overdensity at $2R_{200}$ is quite low, and decreases below the spherical collapse barrier at small σ. Hence, we only fit the mean overdensity with a linear barrier model that allows for $\delta < \delta_c$ and do not report the best-fit parameters for the model defined by Equation (D1). As is clear from the right panel of Figure 10, the excursion set mass function calculated for the linear barrier model fit for the $R = 2R_{200}$ halos does not recover the simulated halo mass function and, therefore, this halo mass definition does not improve the success of the excursion set ansatz.

Lastly, as in the discussion in Section 3, one might wonder whether the disagreement between the simulation and excursion set mass functions simply involves a normalization issue. In fact, the normalization and shape of each of the excursion set mass functions differ from the mass function constructed from the simulated halo abundance. Figure 11 shows $f_{\rm sim}(\nu_c)/f_{\rm fit}(\nu_c)$, the ratio of the first-crossing distribution $f_{\rm sim}(\nu_c)$ determined from the simulations to $f_{\rm fit}(\nu_c)$, the first-crossing distribution calculated using the linear barrier model fits to the overdensity distribution, for each of the halo mass definitions considered in this paper ($\Delta = 100$, $\Delta = 200$, and $\Delta = 600$ spherical overdensities, FOF halos, and halos with masses determined by the particle distribution within a radius $R = 2R_{200}$ of the halo center-of-mass). For the $\Delta = 200$ and $\Delta = 600$ halo definitions, Figure 11 shows the ratio of the best-fit analytical Tinker et al. (2008) and excursion set first-crossing distributions. For the other halo definitions, the binned first-crossing distribution determined by the simulated halo mass function is divided by

the excursion set first-crossing distribution at the appropriate ν_c value. Uncertainty estimates for $f_{\rm sim}(\nu_c)/f_{\rm fit}(\nu_c)$ for these halo mass definitions (the error bars in Figure 11) have the same fractional error as for the first-crossing distributions plotted in Figures 8–10. For each mass definition, $f_{\rm sim}/f_{\rm fit}$ varies with the peak height ν_c and demonstrates that the disagreement between the simulated and excursion set first-crossing distributions does not owe simply to their relative normalization.

REFERENCES

Audit, E., Teyssier, R., & Alimi, J.-M. 1997, A&A, 325, 439
Bardeen, J. M., Bond, J. R., Kaiser, N., & Szalay, A. S. 1986, ApJ, 304, 15
Bardeen, J. M., Steinhardt, P. J., & Turner, M. S. 1983, Phys. Rev. D, 28, 679
Bertschinger, E., & Jain, B. 1994, ApJ, 431, 486
Blumenthal, G. R., Faber, S. M., Primack, J. R., & Rees, M. J. 1984, Nature, 311, 517
Bond, J. R., Cole, S., Efstathiou, G., & Kaiser, N. 1991, ApJ, 379, 440
Bond, J. R., & Myers, S. T. 1996, ApJS, 103, 1
Chandrasekhar, S. 1943, Rev. Mod. Phys., 15, 1
Chiueh, T., & Lee, J. 2001, ApJ, 555, 83
Cohn, J. D., & White, M. 2008, MNRAS, 385, 2025
Cole, S., & Kaiser, N. 1989, MNRAS, 237, 1127
Cuesta, A. J., Prada, F., Klypin, A., & Moles, M. 2008, MNRAS, 389, 385
Dalal, N., White, M., Bond, J. R., & Shirokov, A. 2008, ApJ, 687, 12
Davis, M., Efstathiou, G., Frenk, C. S., & White, S. D. M. 1985, ApJ, 292, 371
Del Popolo, A., Ercan, E. N., & Xia, Z. 2001, AJ, 122, 487
Desjacques, V. 2008, MNRAS, 388, 638
Doroshkevich, A. G. 1970, Astrofizika, 6, 581
Dunkley, J., et al. 2008, ApJS, 180, 306
Efstathiou, G., Frenk, C. S., White, S. D. M., & Davis, M. 1988, MNRAS, 235, 715
Eisenstein, D. J., & Hu, W. 1998, ApJ, 496, 605
Eisenstein, D. J., & Loeb, A. 1995, ApJ, 439, 520
Eke, V. R., Cole, S., & Frenk, C. S. 1996, MNRAS, 282, 263
Gao, L., Springel, V., & White, S. D. M. 2005, MNRAS, 363, L66
Governato, F., Babul, A., Quinn, T., Tozzi, P., Baugh, C. M., Katz, N., & Lake, G. 1999, MNRAS, 307, 949
Gross, M. A. K., Somerville, R. S., Primack, J. R., Holtzman, J., & Klypin, A. 1998, MNRAS, 301, 81
Gunn, J. E., & Gott, J. R. I. 1972, ApJ, 176, 1
Guth, A. H., & Pi, S.-Y. 1982, Phys. Rev. Lett., 49, 1110
Harker, G., Cole, S., Helly, J., Frenk, C., & Jenkins, A. 2006, MNRAS, 367, 1039
Hoffman, Y. 1986, ApJ, 308, 493
Hu, W., & Kravtsov, A. V. 2003, ApJ, 584, 702
Jenkins, A., Frenk, C. S., White, S. D. M., Colberg, J. M., Cole, S., Evrard, A. E., Couchman, H. M. P., & Yoshida, N. 2001, MNRAS, 321, 372
Jing, Y. P. 1998, ApJ, 503, L9
Jing, Y. P. 1999, ApJ, 515, L45
Jing, Y. P., Suto, Y., & Mo, H. J. 2007, ApJ, 657, 664
Kaiser, N. 1984, ApJ, 284, L9
Katz, N., Quinn, T., & Gelb, J. M. 1993, ApJ, 265, 689
Kauffmann, G., Colberg, J. M., Diaferio, A., & White, S. D. M. 1999, MNRAS, 303, 188
Kravtsov, A. V., Klypin, A. A., & Khokhlov, A. M. 1997, ApJS, 111, 73
Lacey, C., & Cole, S. 1993, MNRAS, 262, 627
Lacey, C., & Cole, S. 1994, MNRAS, 271, 676
Lee, J., & Shandarin, S. F. 1998, ApJ, 500, 14
Lee, J., & Shandarin, S. F. 1999, ApJ, 517, L5
Li, Y., Mo, H. J., & Gao, L. 2008, MNRAS, 389, 1419
Lifshitz, E. M. 1946, J. Phys. USSR, 10, 116
McDonald, P., et al. 2006, ApJS, 163, 80
Mo, H. J., & White, S. D. M. 1996, MNRAS, 282, 347
Monaco, P., Theuns, T., & Taffoni, G. 2002, MNRAS, 331, 587
Nariai, H., & Fujimoto, M. 1972, Prog. Theor. Phys., 47, 105
Peebles, P. J. E. 1965, ApJ, 142, 1317
Peebles, P. J. E. 1980, The Large-Scale Structure of the Universe (Princeton, NJ: Princeton Univ. Press)
Peebles, P. J. E. 1982, ApJ, 263, L1
Percival, W. J., et al. 2007, ApJ, 657, 645
Porciani, C., Catelan, P., & Lacey, C. 1999, ApJ, 513, L99
Press, W. H., & Schechter, P. 1974, ApJ, 187, 425
Reed, D. S., Bower, R., Frenk, C. S., Jenkins, A., & Theuns, T. 2009, MNRAS, 394, 624
Rees, M. J., & Ostriker, J. P. 1977, MNRAS, 179, 541
Sachs, R. K., & Wolfe, A. M. 1967, ApJ, 147, 73
Sandvik, H. B., Möller, O., Lee, J., & White, S. D. M. 2007, MNRAS, 377, 234
Seljak, U., & Warren, M. S. 2004, MNRAS, 355, 129
Shen, J., Abel, T., Mo, H. J., & Sheth, R. K. 2006, ApJ, 645, 783
Sheth, R. K., Mo, H. J., & Tormen, G. 2001, MNRAS, 323, 1
Sheth, R. K., & Tormen, G. 1999, MNRAS, 308, 119
Sheth, R. K., & Tormen, G. 2002, MNRAS, 329, 61
Sheth, R. K., & Tormen, G. 2004, MNRAS, 350, 1385
Spergel, D. N., et al. 2003, ApJS, 148, 175
Spergel, D. N., et al. 2007, ApJS, 170, 377
Starobinsky, A. A. 1983, Sov. Astron. Lett., 9, 302
Tinker, J., Kravtsov, A. V., Klypin, A., Abazajian, K., Warren, M., Yepes, G., Gottlöber, S., & Holz, D. E. 2008, ApJ, 688, 709
Tormen, G. 1998, MNRAS, 297, 648
Wang, H. Y., Mo, H. J., & Jing, Y. P. 2007, MNRAS, 375, 633
Warren, M. S., Abazajian, K., Holz, D. E., & Teodoro, L. 2006, ApJ, 646, 881
Wechsler, R. H., Bullock, J. S., Primack, J. R., Kravtsov, A. V., & Dekel, A. 2002, ApJ, 568, 52
Wechsler, R. H., Zentner, A. R., Bullock, J. S., Kravtsov, A. V., & Allgood, B. 2006, ApJ, 652, 71
Wetzel, A. R., Cohn, J. D., White, M., Holz, D. E., & Warren, M. S. 2007, ApJ, 656, 139
White, S. D. M., Efstathiou, G., & Frenk, C. S. 1993, MNRAS, 262, 1023
White, S. D. M., & Rees, M. J. 1978, MNRAS, 183, 341
Zel'dovich, Y. B. 1970, A&A, 5, 84
Zentner, A. R. 2007, Int. J. Mod. Phys. D, 16, 763
Zhang, J., & Hui, L. 2006, ApJ, 641, 641